UNIVERSITY OF OKLAHOMA

GRADUATE COLLEGE

TEST OF DIFFERENT TRANSFORMATION FUNCTIONS TO HYDROMETEOR AND WATER VAPOR MIXING RATIOS FOR DIRECT VARIATIONAL ASSIMILATION OF RADAR REFLECTIVITY DATA

A THESIS

SUBMITTED TO THE GRADUATE FACULTY

in partial fulfillment of the requirements for the

Degree of

MASTER OF SCIENCE IN METEOROLOGY

By

JIAFEN HU
Norman, Oklahoma
2021

TEST OF DIFFERENT TRANSFORMATION FUNCTIONS TO HYDROMETEOR AND WATER VAPOR MIXING RATIOS FOR DIRECT VARIATIONAL ASSIMILATION OF RADAR REFLECTIVITY DATA

A THESIS APPROVED FOR THE
SCHOOL OF METEOROLOGY

BY THE COMMITTEE CONSISTING OF

Dr. Guifu Zhang, Chair

Dr. Jidong Gao, Co-Chair

Dr. Pam Heinselman

Dr. Feng Xu

Acknowledgements

First and foremost, I would like to express my sincere gratitude to my research adviser Dr. Jidong Gao who gives me the opportunity to do this work and provides very invaluable and comprehensive guidance throughout my research. This research project not only allowed me to learn more about data assimilation, especially three-dimensional variational data assimilation method, but also improved my programming skills a lot. I would like to express my gratitude to Dr. Guifu Zhang for being my committee chair, and Drs. Pam Heinselman and Feng Xu for being my committee members and their sacrifice for attending my defense in the final weeks.

I would also like to thank Sijie, Haiqin, Muyun and Anwei. They were very willing to help me and available for questions whenever I asked them. It's a great honor to work with them and to be a part of this research group. I'd like to thank Dr. Chengsi Liu for attending our weekly meeting and providing many useful suggestions on how to solve some technical problems throughout my research. I'd also like to thank my friend Qing Niu who is also a master student in School of Meteorology. We came to OU at same time, and she was always happy to help me no matter on courses or in life.

In the end, I am extremely thankful to my parents for their understanding, love and always supporting me. Although I cannot accompany them, they didn't blame me and gave me a lot of encouragements. And I'd like to thank my boyfriend Huanhuan for his love and support. He not only helped me on my research work but also took care of me in life.

Table of Contents

List of Tables

List of Figures

Abstract

Many issues exist when using highly nonlinear radar reflectivity forward observation operator in three-dimensional variational data assimilation methods (3DVAR), especially with hydrometeor mixing ratios as control variables (denoted as Q). One of the outstanding problems is when hydrometeor mixing ratios from the model background are very small, the cost function gradient can be extremely large, which causes slow convergence. In order to solve this problem, two methods were recently proposed. One uses logarithmic hydrometeor mixing ratios (LOGQ) as control variables during minimization process. Another uses power transformed mixing ratios (PQ), which applies a power parameter p to the variable transformation, as new control variables.

In this study, all three methods are implemented in a weather adaptive, high-resolution, deterministic Warn-on-Forecast analysis and forecast system and tested on three severe weather events that occurred during the Hazardous Weather Testbed (HWT) spring experiment period in May 2019. Radar reflectivity and radial velocity are assimilated along with pseudo-water vapor observations derived from vertically integrated liquid water. The power transformation function is also applied on water vapor mixing ratios to test the impact. Both qualitative and quantitative evaluation are performed on 0–3-hour forecasts launched hourly from 1900 to 2300 UTC for each of the 3 cases. It is found that analysis performance in experiments with PQ and LOGQ as control variables are better than those experiments with Q. The convergence rate of cost function minimization with PQ is faster than the experiments with Q. It is also found spurious analysis increments are produced in experiments with Q and LOGQ sometimes. Using PQ as control variables can alleviate this problem which produces less spurious

analysis increment and slightly improves short-term severe forecasts compared to Q as control variables. Applying power transformation function to pseudo-water vapor is shown to have little benefit to the performance of analysis and forecast.

1. Introduction

1.1 Overview of Different Data Assimilation Methods in Convective Scale NWP

With the development of numerical weather prediction (NWP) models, it is important to seek the most accurate estimate of initial conditions to produce better forecast quality. Data assimilation (DA) is a process that combines observations and short-range forecasts to obtain the initial conditions for NWP models. Weather radar observations are very important for convective NWP and can provide sufficient information for convective storms because of their high temporal and spatial resolutions (Lilly, 1990). Therefore, the assimilation of radar data within NWP models can greatly improve analysis and forecasts of convective storms which is proved by numerous studies (Carley, 2012; Gao et al., 1999, 2016; Gao & Stensrud, 2012; Stensrud & Gao, 2010; Tong & Xue, 2005, and many others). There are several DA methods which were used to assimilate radar data in convective scale NWP.

The simplest way to assimilate radar data into convective scale NWP models is through complex cloud analysis schemes which retrieve hydrometers and adjust in-cloud temperature and moisture using radar reflectivity data (Hu et al., 2006a). In this study, Hu et al. (2006) show that the spinup problem of forecasts can be alleviated through a cloud analysis method, which also can reduce spurious storms. When the cloud analysis procedure is combined with radial velocity DA through another analysis scheme, short term forecasts of convective storms can be improved (Hu, et al., 2006b). The cloud analysis approach is efficient for low computational cost, but it is limited by relying on empirical relations that may lose information from the forecast background. Therefore,

the cloud analysis procedure is applied in conjunction with other direct DA method in many studies.

Other radar DA methods mainly include three- or four-dimensional variational DA (3DVAR or 4DVAR), ensemble Kalman filter (EnKF) and hybrid ensemble-variational (EnVar) approaches. Within the variational framework, the goal is to find the desired analysis state by directly minimizing a cost function that measures the distance of the analysis from background forecasts and that from observations (Kalnay, 2003). Many studies demonstrated that 3DVAR has positive impacts on deterministic forecasts of convective storms (Gao et al., 2004; Hu, et al., 2006b; Schenkman et al., 2011; Sugimoto et al., 2009; Xiao et al., 2005). Gao et al. (2004) developed a 3DVAR approach which included a mass continuity equation as a weak constraint. The method was mainly used to assimilate radar data for convective scale NWP. It has been shown that the use of mass continuity equation as a weak constraint is beneficial for dual-Doppler radar wind analysis (Gao et al. 2013a). The system was designed for convective-scale radar DA at the Center for Analysis and Prediction of Storms (CAPS; Gao et al., 1999, 2004; Ge et al., 2010; Hu et al., 2006a, b) and further improved at National Severe Storms Laboratory (Stensrud and Gao, 2010; Gao and Stensrud 2012, 2016).

Gao and Stensrud (2012) proposed a new radar reflectivity forward operator based on a cycled 3DVAR system. The new forward operator uses a hydrometeor classification algorithm provided by the background temperature field from NWP model. Results showed that the spinup problem can be alleviated when both radial velocity and reflectivity data are assimilated, and the analyses of convective storms are greatly improved with hydrometer classification. Instead of applying a hydrometer classification

algorithm to the reflectivity observation operator, Liu et al. (2019) introduced temperature-dependent background error profiles to classify radar-observed precipitation information based on the 3DVAR method. When the background errors are homogenous, unphysical analysis increments of hydrometeors occur and spread vertically. This issue can be reduced when using the new temperature-dependent background error profiles. Lai et al. (2019) retrieved pseudo-water vapor mass mixing ratios from deep moist convection areas identified by vertically integrated liquid water, which is derived from radar reflectivity data. Therein, it is demonstrated that both analyses and forecasts of convective storms are improved when pseudo-water vapor observations are assimilated along with radar radial velocity and reflectivity within the 3DVAR framework. In Sugimoto et al. (2009), the radar radial velocity and reflectivity data are assimilated by using the Weather Research and Forecasting (WRF) model 3DVAR combined with a cloud analysis scheme. The study indicated that the radar reflectivity assimilation is helpful for strong precipitation areas and using multiple Doppler radars can be beneficial for recovering the full wind component, which is very important within the 3DVAR framework.

The 4DVAR approach, contrast to 3DVAR, adds a time dimension to the cost function that allows a comparison between the model state and the observations at the appropriate time. Furthermore, the goal of 4DVAR is to find an initial condition that enables the forecast to best fit the observations within the assimilation interval. In Sun et al. (1991) the full three-dimensional wind and temperature fields are recovered from single-Doppler radar data using a new proposed method within 4DVAR framework. The study demonstrated that the method is successful in retrieving unobserved velocity

components and temperature, but it works only for dry boundary layers. In order to assimilate data from single or multiple Doppler radars, Sun and Crook (1997) developed a variational Doppler radar analysis system (VDRAS) using a 4DVAR DA technique with a warm rain parameterization scheme. They compared the performance of directly assimilating radar reflectivity and assimilating rainwater mixing ratio retrieved from reflectivity data. Results showed that assimilating retrieved rainwater performed better than direct assimilation of reflectivity.

Wang et al. (2013) later applied a 4DVAR method to the WRF model to assimilate radar data and found that the WRF 4DVAR system can improve short-term quantitative precipitation forecasting (QPF) skills. Sun and Wang (2013) used a Great Plains squall line case to compare the QPF skill of the WRF 4DVAR system with the WRF 3DVAR system. They found that the 4DVAR system improved convective-scale initial conditions, resulting in better QPF skill than the 3DVAR scheme. Although there are many advantages to implementing 4DVAR for radar DA, this approach has limitations when applied to warm rain microphysical processes.

Apart from variational methods, the application of the EnKF technique to radar DA has shown to be effective with its own advantages. The primary problem of 3DVAR is that the background error covariance is static and non-flow-dependent, which can be solved by using an ensemble-based background error covariance adopted in the EnKF method. Since there is not required for tangent linear or adjoint models because of evolving forecast error covariance within EnKF, the nonlinearity of observation operator which is an issue in 3DVAR framework can be easily technically handled. However, the problem still exists theoretically.

Tong and Xue (2005) developed a Doppler radar DA system based on EnKF and tested it by using simulated radar data. The study showed that the EnKF method was effective in retrieving multiple microphysical species with the adaption of complex multiclass ice microphysics and in retrieving wind and thermodynamic variables. It was noted that when both radial velocity and reflectivity were assimilated, the simulated storm could be well reconstructed. They also pointed out that using ensemble-based and flow-dependent background error covariances had positive impacts on radar DA.

The large inherent uncertainty due to the impossibility of representing precipitation particle parameters distribution and diversity within single-moment microphysics schemes resulted in precipitation uncertainty (Gilmore et al., 2004). Yussouf et al. (2013) further compared single-moment and double-moment microphysics schemes with a combined mesoscale and storm-scale assimilation system based on EnKF. Results showed that good analyses and forecasts can be produced with these microphysics schemes but using a double-moment microphysics scheme generated better reflectivity structure compared to radar observations than a single-moment scheme.

Johnson et al. (2015) examined the performance of convective-scale precipitation forecasts between the GSI-based EnKF and the 3DVAR systems. The results indicated that GSI-based EnKF produced better forecasts of convective storms than the 3DVAR system. In addition, the storms predicted with EnKF method can persist for longer time than that those predicted using the 3DVAR. They concluded that the disadvantages of 3DVAR were due to static background error covariance while EnKF adapted flow-dependent background error covariance. Although both EnKF and 4DVAR methods can

produce promising analyses with warm rain processes (Caya et al., 2005), the EnKF approach systematically outperforms 4DVAR for its easier practical implementation.

To combine the advantages of both variational method and EnKF, the hybrid ensemble-variational (EnVar) approach (Hamill and Snyder, 2000; Lorenc 2003; Buehner 2005; Wang et al. 2007) was proposed, which combines the static and ensemble background error covariances to solve the problem of non-flow-dependent error statistics within the variational framework. This idea was applied to convective scale NWP by Gao et al. (2013b) and Gao and Stensrud (2014) using the extended control variable approach and applied it to the assimilation of simulated Doppler radial velocity and reflectivity for a convective storm. Results have demonstrated that the hybrid method produced similar performance compared to the EnKF-alone method when using single radar data and they both outperformed over the 3DVAR. Additionally, the hybrid method generated smallest rms errors with two radars in comparison with the 3DVAR and EnKF methods and the storm spin-up time can be reduced within hybrid scheme (Gao et al. 2013b). Similarly, Kong et al. (2018) compared a hybrid En3DVar system with 3DVAR, EnKF, and ‘‘deterministic forecast’’ EnKF (DfEnKF) through observing system simulation experiments. They found that the hybrid En3DVar method with a 5%–10% static error covariance provided best results when the ensemble size was larger than 20. However, larger static covariances performed better for smaller ensemble size. It also indicated that EnKF and DfEnKF gave best performance relative to hybrid En3DVar and 3DVAR with 40 ensemble members.

In the above discussion, we have reviewed several popular DA methods used previously for convective scale NWP, especially for assimilating radar data. Theoretically,

4DVAR, EnKF, and the hybrid method are advanced DA methods. However, they are relatively expensive for high-resolution convective scale NWP. In many operational centers, the 3DVAR method is still used because of its high efficiency in convective scale NWP (Simonin, 2014; Brousseau et al., 2016; Gustafsson et al., 2018).

1.2 Review of Previous Studies about Variational Reflectivity Data Assimilation

Gao and Stensrud (2012) proposed a radar reflectivity forward operator based on a cycled 3DVAR system. The forward operator used a hydrometeor classification algorithm provided by background temperature fields from an NWP model. Results showed that the spinup problem can be alleviated when both radial velocity and reflectivity data are assimilated, and the analyses of convective storms are greatly improved with hydrometer classification. Liu et al. (2019) instead adopted temperature-dependent background error profiles to classify radar-observed precipitation information among hydrometeors and solve the problem arose by static background error covariances related to the 3DVAR method. Although the above studies demonstrated that improved reflectivity forward operators were beneficial to the analyses of supercell storms, the main issue of variational reflectivity DA associated with nonlinearity still remained a problem.

As noted previously, Sun and Crook (1997) found that indirectly assimilating rainwater mixing ratio provided better results than assimilating reflectivity directly where a highly nonlinear observation operator introduced nonlinearity to the cost function in the minimization process. They also found when background rainwater mixing ratio is very small, a very large gradient of cost function will occur resulting in difficult minimization

convergence when the nonlinear forward operator of reflectivity was used (Sun and Crook 1997).

In order to reduce the issue related to nonlinear observation operator, Carley (2012) employed a logarithmic form of hydrometeor mixing ratios as control variables to assimilate radar reflectivity data based on a Gridpoint Statistical Interpolation (GSI) hybrid ensemble-3DVAR system. The study showed that using logarithmic control variables was beneficial for reducing errors generated during the linearization process compared to using mixing ratios themselves as control variables. However, the logarithmic control variables were proved to underestimate the nonlinear reflectivity perturbation, which may produce an overestimated increment of mixing ratio (Carley, 2012).

Alternatively, Wang and Wang (2017) proposed a new method to direct assimilate radar reflectivity without tangent linear and adjoint of the nonlinear observation operator by directly using reflectivity as a control variable based on GSI EnVar system. This approach avoided the problem related to nonlinearity of the reflectivity observation operator when using hydrometeor mixing ratios as control variables, and the problem associated with transformation between standard and logarithmic space when using logarithmic mixing ratios as control variables. Results indicated that employing reflectivity as a state variable produced more consistent results with reality than using standard and logarithmic forms of mixing ratios. However, the background error covariance in this method was fully derived from an ensemble. Therefore, when adopting pure variational or hybrid EnVar systems that include static background covariance, the issue of nonlinearity still exists.

In order to further explore the problems with respect to nonlinear reflectivity operator, Liu et al. (2020) proposed several treatments to alleviate the issues using 3DVAR method through observing system simulation experiments. The treatments included 1) employing lower limits to the mixing ratios or to the equivalent reflectivity, 2) assimilating radar radial velocity and reflectivity data in separate passes and 3) using logarithmic mixing ratios as state variables, implemented with a lower limit and background smoothing. The lower limits treatment was able to avoid large cost function gradient introduced from small background reflectivity. In addition, the study showed that the lower limits imposed on equivalent reflectivity performed better than on mixing ratios. The treatment of separately assimilating radial velocity and reflectivity was found helpful for solving the problem of ineffective assimilation of radial velocity when assimilated together with reflectivity. Furthermore, applying a background smoothing and lower limits to the background mixing ratios, when using logarithmic form of control variables, alleviated the issue of spurious analysis increments generated by this method. Results demonstrated that using logarithmic mixing ratios as control variables, with the several treatments mentioned above, created more consistent analysis with observations, and the convergence processes were faster.

In addition to using logarithmic transformation of control variables, Yang et al. (2020) adopted a nonlinear transformation function to improve variational analysis of visibility and ceiling height based on NCEP's Real-Time Mesoscale Analysis (RTMA) system. The newly proposed transformation function can make non-Gaussian variables become closer to the Gaussian distribution. Additionally, it includes linear and logarithmic functions adjusted by varying a parameter from 0 to 1. Results demonstrated that the experiment

with the application of a nonlinear transformation function produced better analysis of visibility and ceiling height and alleviated the issues related to linear approximation. In a more recent study, the idea of power transformation of control variables was applied to reflectivity DA research by treating the hydrometeor variables as control variables (Cao et al. 2010; Chen et al. 2020). The performance of assimilating radar data using the transformation function was compared with those using hydrometeor mixing ratios and logarithmic mixing ratios as control variables. Results showed that the assimilation of reflectivity with the transformation function gave the best reflectivity forecasts in terms of root-mean-square error and equitable threat score, compared with other two methods.

The previous studies about reflectivity DA discussed above provide a solid foundation for identifying some of the remaining challenges and advancements needed to improve reflectivity DA for convective scale NWP.

1.3 Motivation and Outline

As previously discussed, directly assimilating radar reflectivity in a variational framework has problems associated with highly nonlinear reflectivity observation operator when using hydrometeor mixing ratios as control variables. When hydrometeor mixing ratios from the model background are very small, the cost function gradient can be extremely large, which causes slow convergence and then affects the efficiency of radar data assimilation. So, my study in this thesis will focus on improving radar reflectivity forward observation operator and also applying the power transform function to model water vapor variables so that radar reflectivity data can be effectively assimilated in the variational system. The topic about applying the power transform function to model

water vapor variables is new and has never been studied before. In addition, the idea about pseudo-water vapor assimilation proposed by Lai et al. (2019) will be tested together with the power transform function to see if it benefits the convective scale NWP in the experiment with power transform function applied to hydrometeors.

Based on the above reference review and discussion, though there are several advanced DA methods we can use, we choose a 3DVAR system (Gao et al. 2013) in our current study because of its efficiency. The system was built and implemented for the Warn-on-Forecast project (Gao et al. 2013; Stensrud et al. 2013) and was designed for convective-scale radar DA (Gao et al., 1999, 2004; Ge et al., 2010; Hu et al., 2006a, b; Stensrud and Gao, 2010; Gao and Stensrud 2012).

Several treatments have been proposed in previous studies to solve the problem of nonlinear observation operator (Carley, 2012; Liu et al., 2020). But the problems are not fully solved. Instead of adopting the logarithmic transformation, Yang et al. (2020) applied a nonlinear transformation function to the visibility and ceiling height analysis, which transformed the variables to a more uniform variance space. In this study, we will apply this power transformation function to hydrometeor mixing ratios, which uses a power parameter p to the variable transformation, to see whether this transformation is able to solve the operator nonlinearity problem. The power-transformed mixing ratios form as new control variables to assimilate reflectivity data within the 3DVAR framework. In the first goal of this study is to build this power transformation function into the 3DVAR system developed by Gao et al. (2004, 2013).

In a previous study, the assimilation of pseudo-water vapor, along with radial velocity and reflectivity, had positive impact on the analyses and forecasts of convective

storms (Lai et al., 2019). The newly developed reflectivity forward operator will also be tested along with the pseudo-water vapor observations due to their positive impact. In addition, we will also apply the power transformation to the pseudo-water vapor allowing it to have equivalent magnitude with other hydrometeor control variables so that the solution of the 3DVAR problem may be converged quickly. The performances of newly developed component of the system are examined by using three severe weather events that occurred in May 2019 and the results are compared with those from the previous 3DVAR method which uses the nonlinear reflectivity forward operator. We hope this transformation of control variables can enhance the convergence rate and improve the analyses and short-term severe forecasts.

The rest of this thesis is outlined as follows. Chapter 2 introduces the 3DVAR system, the radial velocity and reflectivity observation operators, the logarithmic and nonlinear power transformation function and the pseudo-observation and assimilation algorithm. The experimental design is presented in Chapter 3. Chapter 4 shows the experiment results of analyses and forecasts with different methods. The discussion and conclusions are provided in Chapter 5. Chapter 6 gives the future works.

2. Methodology

2.1 The 3DVAR system

Lorenc (1986) used Bayesian probabilistic arguments to derive standard equations of variational techniques and assumed Gaussian error distributions. The principle of a variational technique is to find the best analysis for numerical weather prediction by minimizing the cost function. The following description of 3DVAR cost function is followed by Gao et al. (2004) which can be written as

$$J(\boldsymbol{x}) = \frac{1}{2}(\boldsymbol{x} - \boldsymbol{x}^b)^T \boldsymbol{B}^{-1}(\boldsymbol{x} - \boldsymbol{x}^b) + \frac{1}{2}[H(\boldsymbol{x}) - \boldsymbol{y}^o]^T \boldsymbol{R}^{-1}[H(\boldsymbol{x}) - \boldsymbol{y}^o] + J_c(\boldsymbol{x}). \quad (1)$$

The cost function consists of three terms. The first term on the right-hand side which is weighted by the inverse of the background error covariance matrix $\boldsymbol{B}$ measures the distance between the analysis or control vector, $\boldsymbol{x}$, and the background vector, $\boldsymbol{x}^b$.The 3DVAR system assimilates radar radial velocity, reflectivity and surface observations. Thus, there are several variables included in the analysis vector $\boldsymbol{x}$: the wind components (u, v and w), the hydrometeor mixing ratios for rainwater (q_r), snow (q_s) and hail (q_h), pressure (p), potential temperature (θ) and water vapor mixing ratio (q_v). The second term of the cost function is the observation term which determines the distance between the analysis vector, $\boldsymbol{x}$, mapped to the observation locations by the nonlinear forward observation operator $H(\boldsymbol{x})$, and the observation vector, $\boldsymbol{y}^o$, and which is weighted by the inverse of the observation error covariance matrix $\boldsymbol{R}$. The third term, $J_c(\boldsymbol{x})$, is a penalty term which employs the mass continuity equation as a weak constraint (Gao et al., 1999, 2004).

To effectively precondition the minimization problem, we follow Courtier et al. (1994) and Courtier (1997) and define an alternative control variable **v**, such that **C**=

$\sqrt{\mathbf{B}}\mathbf{v} = \left(\mathbf{x} - \mathbf{x}^b\right)$. This allows the cost function (1) to be changed into an incremental form, such that

$$J_{inc}(\mathbf{v}) = \frac{1}{2}\mathbf{v}^T\mathbf{v} + \frac{1}{2}(\mathbf{HC} - \mathbf{d})^T\mathbf{R}^{-1}(\mathbf{HC} - \mathbf{d}) + J_c(\mathbf{v}), \quad (2)$$

where **H** is the linearized version of H and $\mathbf{d} \equiv \mathbf{y}^o - H\left(\mathbf{x}^b\right)$. The gradient and Hessian of J_{inc} can also be derived by differentiating (2) with respect to **v**, yielding,

$$\nabla J_{inc} = (\mathbf{I} + \mathbf{C}^T\mathbf{H}^T\mathbf{R}^{-1}\mathbf{HC})\mathbf{v} - \mathbf{C}^T\mathbf{H}^T\mathbf{R}^{-1}d + \nabla J_c(\mathbf{v}), \quad (3)$$

where **I** is the identity matrix. The Hessian then follows as

$$\nabla^2 J_{inc} = \mathbf{I} + \mathbf{C}^T\mathbf{H}^T\mathbf{R}^{-1}\mathbf{HC} + \nabla^2 J_c(\mathbf{v}). \quad (4)$$

From (4), we can see that the preconditioning prevents the smallest eigenvalue from becoming close to zero. This can improve convergence of minimization algorithms and allows the variational problem to be solved more efficiently.

The **C** defined in (2) can be further broken down as

$$\mathbf{C} = \mathbf{DFL}, \quad (5)$$

where **D** is a diagonal matrix consisting of the standard deviation of background errors and **L** is a scaling factor. The matrix **F** is the square root of a matrix with diagonal elements equal to one, and off diagonal elements equal to the background error correlation coefficients. However, the matrix **F** is too large to be used directly in the minimization calculations. Instead, it is modeled by a spatial recursive filter (Purser et al. 2003).

2.2 Radar forward observation operator

The radar forward observation operator H transforms model state variables (e.g., u, v, q_r, q_s) from model space to observational measurements in observation space (e.g., radial velocity, reflectivity). Both radar radial velocity and reflectivity are assimilated

within 3DVAR framework in this study. The details of the radial velocity and reflectivity forward observation operator are descripted as follows.

2.2.1 **Radial velocity observation operator**

Radar radial velocity data is part of the observation vector $\mathbf{y}^o$ in eq. (1). The radar forward observation operator for radial velocity which includes the effect of earth curvature is written as follows in Doviak and Zrnic (1993) as

$$v_r = \frac{dh}{dr}w + \frac{ds}{dr}(usin\phi + vcos\phi), \tag{6}$$

where v_r is the projected radial velocity, and u, v and w is zonal, meridional and vertical components of the wind; r is the slant range (ray path distance), h is the height above the curving earth's surface, s is the distance along the earth's surface, and ϕ is the azimuth angle of the radar beam direction.

2.2.2 **Reflectivity observation operator**

The assimilation of radar reflectivity by using variational methods is challenging due to the highly nonlinear reflectivity observation operator. The forward observation operator for radar reflectivity (Z in dBZ) can be written as:

$$Z = 10log_{10}(Z_e), \tag{7}$$

where Z_e is the equivalent radar reflectivity factor in linear units (mm^6m^{-3}) obtained from the sum of three hydrometeor species (rainwater, snow and hail), according to the following formulation (Dowell et al., 2011; Gilmore et al., 2004; Y.-L. Lin et al., 1983):

$$Z_e = Z_e(q_r) + Z_e(q_s) + Z_e(q_h). \tag{8}$$

In Eq. (8), $Z_e(q_r)$, $Z_e(q_s)$ and $Z_e(q_h)$ represent the equivalent radar reflectivity factors contributed from rainwater, snow and hail, respectively. The above equation is consistent with the Thompson microphysics parameterization scheme implemented within the WRF

model and used in this study. The Thompson microphysics parameterization scheme predicts the mass mixing ratios for five hydrometeor variables (cloud, ice, rain, snow and hail) and the number concentration for rain and ice.

Based on Smith et al. (1975), the rain component of reflectivity can be calculated from

$$Z_e(q_r) = \frac{10^{18} \times 720(\rho q_r)^{1.75}}{\pi^{1.75} N_r^{0.75} \rho_r^{1.75}}, \quad (9)$$

where $N_r = 8.0 \times 10^6 m^{-4}$ represents the intercept parameter for rain in the Marshall–Palmer exponential raindrop size distribution, ρ (in $kg\ m^{-3}$) is the atmospheric density and $\rho_r = 1000\ kg\ m^{-3}$ represents rainwater density. After plugging in the default values of intercept parameter and the rainwater density, the equation of the equivalent radar reflectivity factor contributed from rainwater (Eq. 9) can be further simplified as

$$Z_e(q_r) = 3.63 \times 10^9 (\rho q_r)^{1.75}. \quad (10)$$

Snow can be divided into dry snow and wet snow. The reflectivity factor from dry snow when the temperature is less than 0℃ is

$$Z_e(q_s) = \frac{10^{18} \times 720 K_i^2 \rho_s^{0.25} (\rho q_s)^{1.75}}{\pi^{1.75} K_r^2 N_s^{0.75} \rho_i^2}, \quad (11)$$

where $K_i^2 = 0.176$ is the ice dielectric factor and $K_r^2 = 0.93$ is the dielectric factor for rainwater, $N_s = 3.0 \times 10^6 m^{-4}$ represents the intercept parameter for snow, $\rho_s = 100\ kg\ m^{-3}$ is the snow density and $\rho_i = 917\ kg\ m^{-3}$ is the same for ice. The simplified form of Eq. (11) based on the default values can be simplified as

$$Z_e(q_s) = 9.80 \times 10^8 (\rho q_s)^{1.75}. \quad (12)$$

If the temperature is higher than 0℃, the component of the equivalent reflectivity factor for wet snow, similar as rainwater, is calculated from

$$Z_e(q_s) = \frac{10^{18} \times 720(\rho q_s)^{1.75}}{\pi^{1.75} N_s^{0.75} \rho_s^{1.75}}. \tag{13}$$

It can be further simplified as,

$$Z_e(q_s) = 4.26 \times 10^{11} (\rho q_s)^{1.75}. \tag{14}$$

For hail, the reflectivity formulation based on Smith et al. (1975) is employed with

$$Z_e(q_h) = \left(\frac{10^{18} \times 720}{\pi^{1.75} N_h^{0.75} \rho_h^{1.75}} \right)^{0.95} (\rho q_h)^{1.6625}, \tag{15}$$

where $\rho_h = 913\ kg\ m^{-3}$ is the hail density and $N_h = 4.0 \times 10^4 m^{-4}$ represents the intercept parameter for hail. Here, the value of N_h is slightly larger than that used in Smith et al. (1975), which implies hail at smaller sizes occur more frequently. Then the simplified equation for hail is

$$Z_e(q_h) = 4.33 \times 10^{10} (\rho q_h)^{1.66}. \tag{16}$$

The radar reflectivity forward observation operators mentioned above are highly nonlinear which may cause the large gradient of the cost function when background mixing ratios are very small (Sun et al. 1997; Liu et al., 2020). The explanation is described as follows.

The linear approximation of reflectivity operator with respect to the rainwater mixing ratio based on Eqs. (7)-(16) is

$$\frac{\partial Z}{\partial q_r} = \frac{\partial Z}{\partial Z_e} \frac{\partial Z_e}{\partial q_r} = \frac{6.35 \times 10^{10} \times \rho^{1.75} q_r^{0.75}}{\ln 10 \times Z_e}. \tag{17}$$

The equations for snow and hail mixing ratios are similar as for rainwater which are

$$\frac{\partial Z}{\partial q_s} = \begin{cases} \dfrac{1.715 \times 10^{10} \times \rho^{1.75} q_s^{0.75}}{\ln 10 \times Z_e} & T \le 0℃ \\ \dfrac{7.455 \times 10^{12} \times \rho^{1.75} q_s^{0.75}}{\ln 10 \times Z_e} & T > 0℃ \end{cases}, \tag{18}$$

$$\frac{\partial Z}{\partial q_h} = \frac{7.19 \times 10^{11} \times \rho^{1.66} q_h^{0.66}}{\ln 10 \times Z_e}. \tag{19}$$

When there is only rainwater contributing to reflectivity ($Z_e = Z_e(q_r)$), the linear approximation of reflectivity operator with respect to rainwater mixing ratio (Eq. 17) can be simplified as

$$\frac{\partial Z}{\partial q_r} = \frac{17.5}{\ln 10 \times q_r}. \tag{20}$$

Similar situation can be applied to snow and hail when having snow or hail mixing ratio only. The equations become

$$\frac{\partial Z}{\partial q_s} = \frac{17.5}{\ln 10 \times q_s}, \tag{21}$$

$$\frac{\partial Z}{\partial q_h} = \frac{16.6}{\ln 10 \times q_h}. \tag{22}$$

From Eqs. (17)-(22), when the background hydrometeor mixing ratios or the total equivalent reflectivity factor are close to zero, the gradient of reflectivity becomes extremely large which will cause the convergence problem during the minimization process of cost function (Sun and Crook, 1997; Wang and Wang, 2017; Liu et al., 2020).

2.3 Logarithm transformation of hydrometeor mixing ratios

Using hydrometeor mixing ratios themselves as control variables has issues related with very large gradient as illustrated above though some special treatments can be done to avoid this (Sun and Crook 1997; Gao and Stensrud 2012). Another way to avoid this problem is by using logarithmic mixing ratios as the control variables (Carley, 2012; Wang and Wang, 2017). The logarithm transformation can be expressed as

$$\hat{q} = \log_{10}(q), \tag{23}$$

where $\hat{q}$ denotes the transformed hydrometeor variables including $\hat{q}_r$, $\hat{q}_s$ and $\hat{q}_h$. Therefore, the equivalent reflectivity factors for rainwater, snow and hail become, respectively,

$$Z_e(\hat{q}_r) = 3.63 \times 10^9 \left(\rho 10^{\hat{q}_r}\right)^{1.75}, \tag{24}$$

$$Z_e(\hat{q}_s) = \begin{cases} 9.80 \times 10^8 \left(\rho 10^{\hat{q}_s}\right)^{1.75} & T \le 0℃ \\ 4.26 \times 10^{11} \left(\rho 10^{\hat{q}_s}\right)^{1.75} & T > 0℃ \end{cases}, \tag{25}$$

$$Z_e(\hat{q}_h) = 4.33 \times 10^{10} \left(\rho 10^{\hat{q}_h}\right)^{1.66}. \tag{26}$$

Then, the total equivalent reflectivity factor is

$$Z_e = Z_e(\hat{q}_r) + Z_e(\hat{q}_s) + Z_e(\hat{q}_h). \tag{27}$$

According to Eq. (7), the logarithm transformation allows the relation between reflectivity and $\hat{q}$ become linear, at least when there only one hydrometeor variable exists.

The linear approximation or the gradient of radar reflectivity forward observation operator when using logarithmic mixing ratios as control variables can be derived as

$$\frac{\partial Z}{\partial \hat{q}_r} = \frac{17.5 \times Z_e(\hat{q}_r)}{Z_e}, \tag{28}$$

$$\frac{\partial Z}{\partial \hat{q}_s} = \frac{17.5 \times Z_e(\hat{q}_s)}{Z_e}, \tag{29}$$

$$\frac{\partial Z}{\partial \hat{q}_h} = \frac{16.6 \times Z_e(\hat{q}_h)}{Z_e}. \tag{30}$$

If there is only one hydrometeor species contributing to the reflectivity (i.e., $Z_e(\hat{q}_r) = Z_e$), the gradient of the reflectivity becomes a constant value from Eqs. (28)-(30). If considering more than one hydrometeor species, the gradient variates corresponding to different value of reflectivity and is likely less than 17.5 dBZ $[\log(kgkg^{-1})]^{-1}$.

Therefore, the logarithm transformation can alleviate the issue with possible very large gradient of the cost function.

However, new problems arise when transforming the analysis increments from logarithm space back to the standard space. The problem can be illustrated with the single-observation analysis which is located at grid point j (Liu et al., 2020). Then the relationship between background error correlation in normal control variables space ρ and in logarithm control variables space $\hat{\rho}$ at grid points i and j can be written as

$$\rho_{ij} = \frac{\delta q_i}{\delta q_j} = \frac{\left[1 + \sum_{k=2}^{\infty} (\ln 10)^{k-1} \delta \hat{q}_i^{k-1} (k!)^{-1}\right]}{\left[1 + \sum_{k=2}^{\infty} (\ln 10)^{k-1} \delta \hat{q}_j^{k-1} (k!)^{-1}\right]} \times \frac{q_{b_i}}{q_{b_j}} \times \hat{\rho}_{ij}, \tag{31}$$

where δq represents the analysis increment of q, and $\delta \hat{q}$ is for $\hat{q}$; q_b is the background in q space. Details for how to derive this equation can be found in Liu et al. (2020).

Based on Eq. (31), if the background error correlation is Gaussian-like in logarithm space, the spatial correlation function in q space is almost Gaussian-like only if the analysis increments in $\log(q)$ space are very small and the background is homogeneous ($q_{b_i} = q_{b_j}$). When the analysis increments of $\log(q)$ are not very small or the background is not homogeneous, the background error correlation in q space is no longer Gaussian-shaped, which will result in spurious analysis increments of q.

In order to solve the problem with spurious analysis increments when transforming the analysis increments from logarithm space back to the q space, Liu et al. (2020) applied a background smoothing and a lower limit treatments to the background mixing ratios. Wang and Wang (2017) used reflectivity directly as control variables in addition to hydrometeor mixing ratios in logarithm space. While both methods help to mitigate these issues, the problems still exist, especially it is difficult to get rid of spurious cells.

2.4 Power transformation of hydrometeor mixing ratios

Instead of using logarithmic hydrometeor mixing ratios as control variables, Yang et al. (2020) proposed a nonlinear power transformation function to improve variational analysis of visibility and ceiling height. This power transformation function is applied to the hydrometeor mixing ratios in this study which can be defined as

$$\hat{q} = \frac{(q^p - 1)}{p} \quad (0 < p \leq 1), \tag{32}$$

where $\hat{q}$ denotes the power transformed hydrometeor mixing ratios and p represents a parameter which is larger than zero and smaller than or equal to 1. When p equals to 1, this equation becomes

$$\hat{q} = q - 1, \tag{33}$$

which is a linear relationship between q and $\hat{q}$. The nonlinearity of the equation grows along with the decrease of p value. When p approaches zero, this transformation function becomes a natural logarithm function. Fig. 2.1 (taken from Fig. 1 in Chen et al. 2020) shows the variability of this function with different p values. Thus, the nonlinear power transformation allows a range of possibility for including both linear and logarithmic functions at each end of the parameter range.

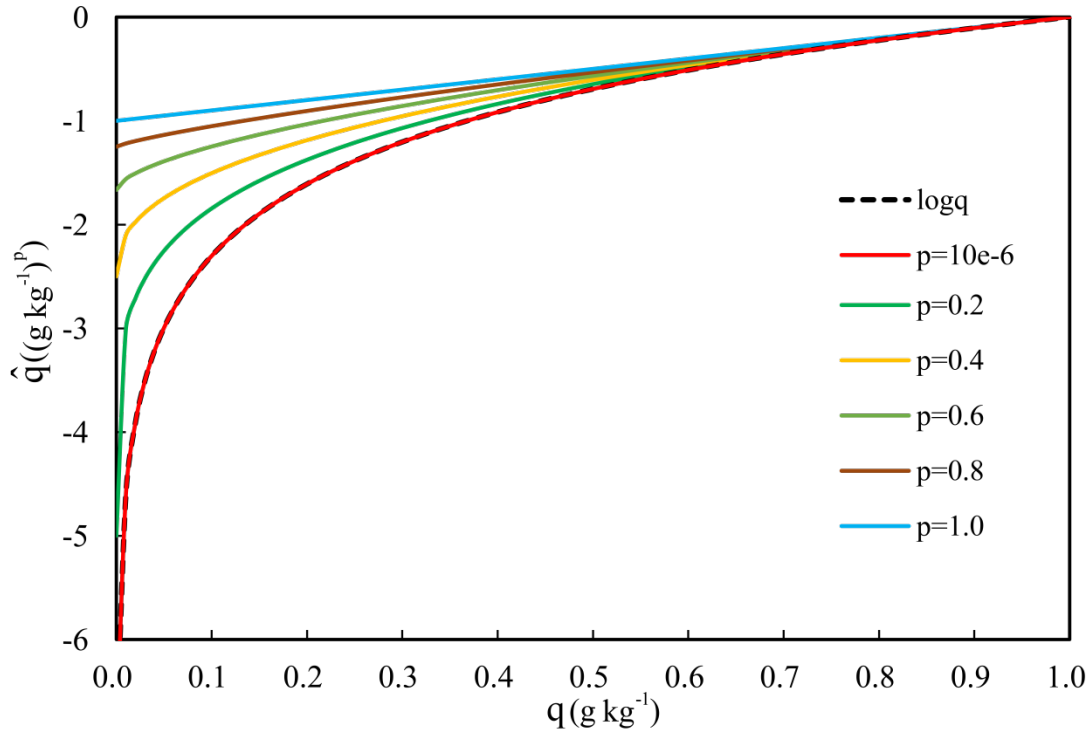

Figure 2.1: The natural logarithm function and the nonlinear transformation function with different parameter p (Chen et al., 2020).

Therefore, the equivalent reflectivity factors for rainwater after power transformation can be written as follows:

$$Z_e(\hat{q}_r) = 3.63 \times 10^9 \left[\rho(p\hat{q}_r + 1)^{\frac{1}{p}}\right]^{1.75}. \quad (34)$$

In addition, $\hat{q}$ needs to be greater than $-1/p$ to avoid negative value when transforming back to the standard space.

Chen et al. (2020) examined the performance of using power transformed hydrometeor mixing ratios as control variables with different p values. Results indicated that when p equaled to 0.4, the 1-h reflectivity forecasts produced the best performance. Thus, we choose p=0.4 in this study to test different transformation functions.

2.5 Pseudo-water vapor mixing ratio observations

Some research found that the assimilation of pseudo-water vapor along with radar radial velocity and reflectivity had positive impact on the analyses and forecasts of convective storms (Carlin 2017; Lai et al., 2019). The pseudo-water vapor mixing ratio observations can be produced based on vertically integrated liquid water (VIL), which is derived from reflectivity observations (Lai et al. 2019). The procedures for how to derive the pseudo-observations based on VIL are shown in Fig. 2.2. Details behind each step in the procedures can be found in Lai et al. (2019).

In this study, the pseudo-water vapor is assimilated together with the radar data to further investigate the impact of the pseudo-water vapor on convective scale analyses and short-term forecasts. In addition, we also apply the power transformation function discussed in 2.4 to the pseudo-water vapor to examine if this can improve the analysis of water vapor mixing ratio and also the short-term forecasts.

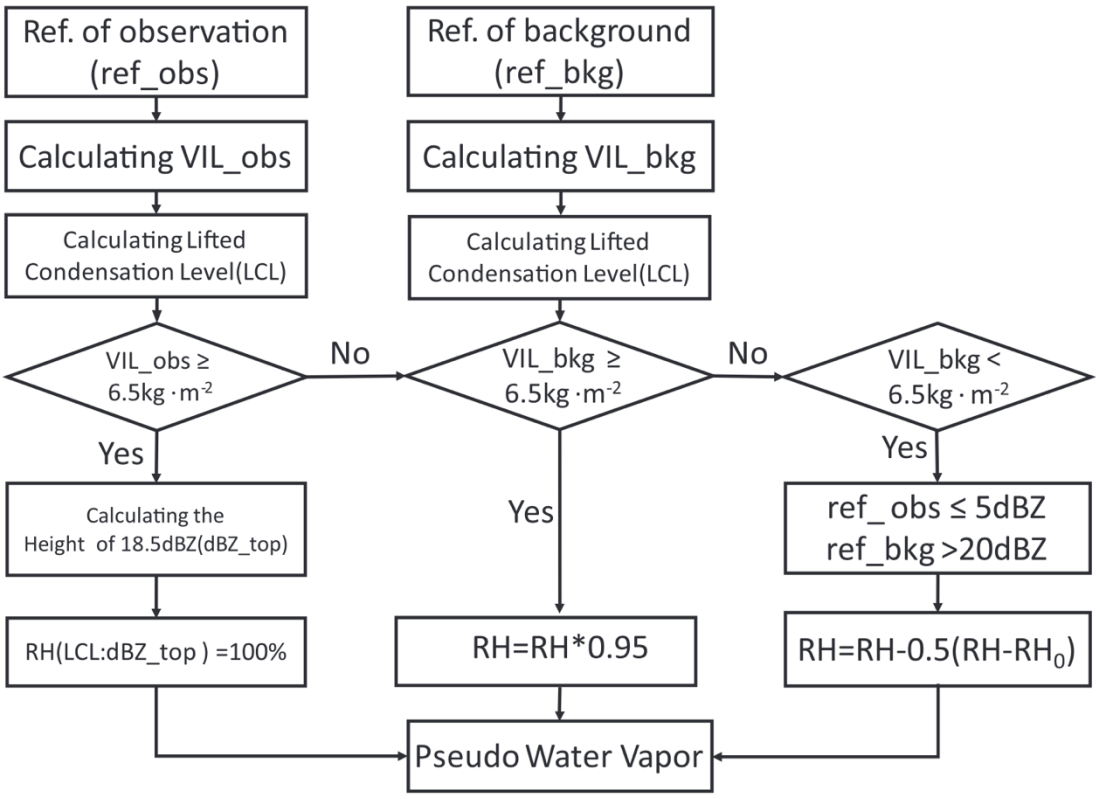

Figure 2.2: Flowchart highlighting the steps for deriving pseudo–water vapor mixing ratio (Lai et al., 2019).

3. Experimental Design

To test the impact of different transformation functions on the assimilation of radar data within an 3DVAR framework, three real data cases are selected from 2019 Warn-on-Forecast (WoF) spring experiments. The forecast model employed in this study is the WRF-ARW model version 3.7.1 which uses the physics configuration including: the Thompson microphysics scheme (Thompson et al., 2008), the Yonsei University (YSU) planetary boundary layer scheme (Hong et al., 2006), the Rapid Radiative Transfer Model for Global circulation models (RRTMG) shortwave and longwave schemes (Iacono et al., 2008) and the unified Noah land surface model (Tewari et al., 2016). The experiment domain for all the cases in this study has 600 × 600 grid points in the horizontal with a grid spacing of 1.5km, and 41 vertical levels.

The flowchart of the cycled DA and forecast experiments is shown in Fig. 3.1. The experiments are cold started at 1900 UTC and extend to 2300 UTC where the 3-km High-Resolution Rapid Refresh (HRRR) forecast fields provide the initial background for the DA cycles and the lateral boundary conditions for forecasts. The radar observations downloaded from the NEXRAD Level-II data at the National Centers for Environmental Information repository (https://www.ncdc.noaa.gov/nexradinv/) are assimilated every 15 minutes during the 4-h cycling period, and the conventional observations (e.g., soundings, surface stations) are assimilated hourly at 1900, 2000, 2100, 2200 and 2300 UTC. Started from 2000 UTC, 3-h forecasts are launched hourly until 2300 UTC.

Five experiments are performed for each case in this study labeled as Q, Q_qv, LOGQ_qv, PQ_qv and PQ_Pqv. Symbols Q, LOGQ and PQ represent using hydrometeor mixing ratios themselves, logarithmic and power transformed hydrometeor mixing

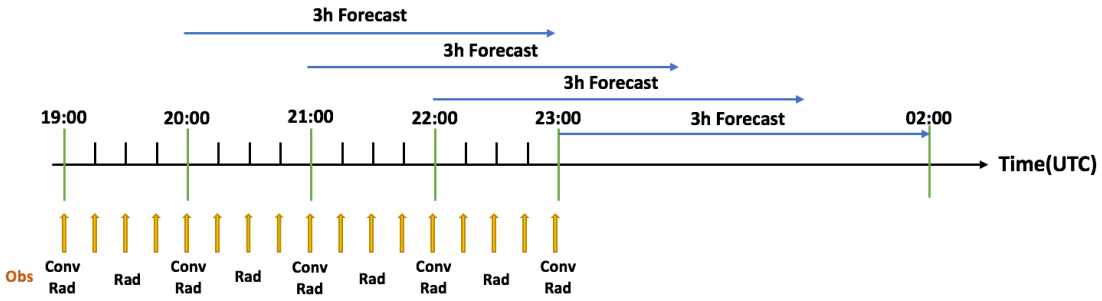

Figure 3.1: Illustration of cycled DA and forecast experiments. "Obs" represents the assimilated observations including conventional observations (Conv) and radar observations (Rad). The yellow arrows show the times when the observations are assimilated. The radar observations are assimilated with 15 min intervals while the conventional observations are assimilated every hour.

ratios, respectively, as control variables. "qv" indicates the pseudo-water vapor observations are assimilated together with radar data, while "Pqv" represents that the power transformation is also applied to pseudo-water vapor mixing ratios to form as new control variables. The detailed descriptions of the experiments are provided in Table 3.1. Experiment Q serves as the control experiment, or the benchmark experiment by using the original hydrometeor variables as part of control variables and assimilating radar reflectivity and radial velocity data, but without assimilating pseudo-water vapor. Experiment Q_qv also uses the original hydrometeor variables as part of the control variables but assimilates pseudo-water vapor in addition to radar reflectivity and radial velocity. Same as Q_qv, however, LOGQ_qv uses the logarithmic function of hydrometeors and PQ_qv uses the power transformation function of hydrometeors as part of the control variables. Finally, experiment PQ_Pqv uses the power transformation function of both hydrometeors and pseudo-water vapor as control variables with the assimilation of both radar data and pseudo-water vapor observations. Five experiments are divided into the following three groups for comparisons and discussions.

Firstly, Experiments Q and Q_qv are compared to investigate the impact of the pseudo-water vapor on convective scale analysis and short-term forecasts. Secondly, Experiments labeled as Q_qv, LOGQ_qv and PQ_qv are compared to test the impact of different transformation functions on the assimilation of radar observations. Finally, PQ_qv with PQ_Pqv are discussed to test the impact of power transformation function on pseudo-water vapor by using power transformed qv as control variables.

Experiment name	Control variables	Description
Q	q	Exp. with q as control variables
Q_qv	q, qv	Exp. with q, qv as control variables
LOGQ_qv	logq, qv	Exp. with logq, qv as control variables
PQ_qv	Pq, qv	Exp. with Pq, qv as control variables
PQ_Pqv	Pq, Pqv	Exp. with Pq, Pqv as control variables

Table 3.1: Description of experiments.

4. Results

4.1 Overview of the 22 May 2019 case

The first case selected for this study occurred on May 22, 2019. Environmental conditions were favorable for the development of tornadoes and severe thunderstorms across the northeast Oklahoma and Missouri. Early in the afternoon, isolated intense thunderstorms existed in southwest and central Oklahoma. Thunderstorms developed across northeast Oklahoma, southeast Kansas, central and southwest Missouri that produced several tornadoes and widespread large hail (3 inches in diameter likely; Fig. 4.1). Then the storms spread northeastward through the evening which persisted into the early overnight period and then weakened somewhat. In all, 47 tornadoes were reported ranging from EF0 to EF3, and 16 of them occurred in Oklahoma.

The simulation domain for 22 May 2019 case includes most of Kansas, Oklahoma, Arkansas, and Missouri (Figs. 4.1, 4.2).

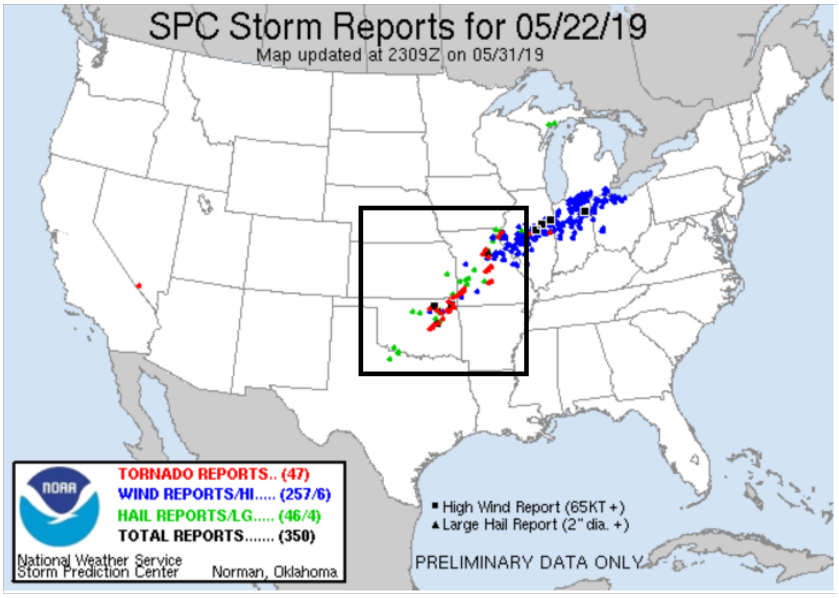

Figure 4.1: The storm reports of 22 May 2019 from the Storm Prediction Center. The black square box represents the simulation domain of the experiments for this case.

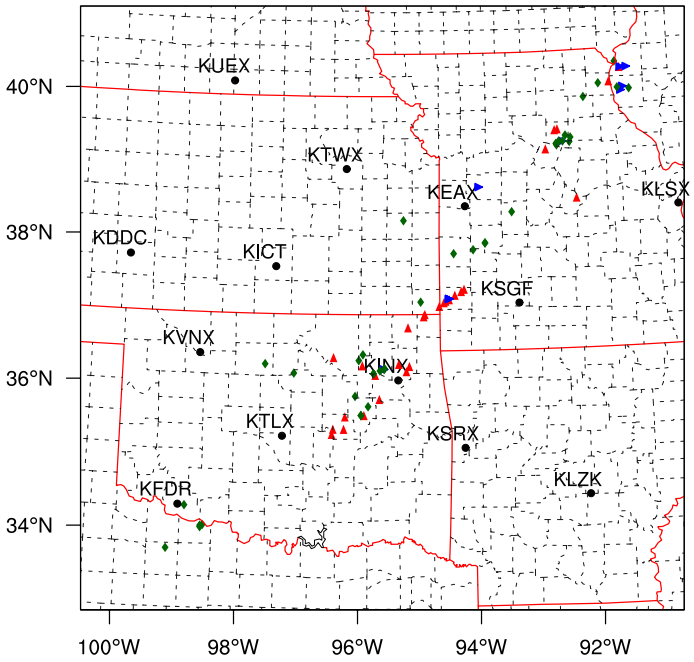

Figure 4.2: The simulation domain and locations of the radar sites for 22 May 2019. The red triangles, green rhombuses and blue triangles indicate the observed tornadoes, hail and wind events from SPC storm reports, respectively. The geographical center of the model simulation domain is at (37.09°N, 95.60°W).

4.1.1 **Results from comparison of experiments Q with Q_qv**

The 1-3 h predicted composite reflectivity fields from experiments Q and Q_qv initiated at 2300 UTC and corresponding observed composite reflectivity are compared (Fig. 4.3) to investigate the impact of assimilating pseudo-water vapor observations along with radar radial velocity and reflectivity. The observed composite reflectivity fields (Fig. 4.3a, d, g) show that several mesoscale convective systems (MCSs) gradually propagate northeastward with new storm cells continuously forming and developing in the middle and northeast of the simulation domain. To better illustrate the differences between two experiments and the observations, the precipitation system is divided into two main regions labeled as A and B from north to south in the simulation domain (Fig. 4.3a). At 0000 UTC, several convective cells are seen in region B (Oklahoma and Texas border) which gradually weaken when propagating northeastward and finally dissipate by 0200 UTC (Fig. 4.3g). In contrast, the weak storm cells in the region A (north central Oklahoma) at 0000 UTC (Fig. 4.3a) grow and form mature supercells after a few hours.

At 1-h forecast (valid at 0000 UTC), the convective cells in region B are absent from experiment Q (Fig. 4.3b) but are predicted in Q_qv (Fig. 4.3c). In addition, the cells in region A are stronger in Q_qv (Fig. 4.3c) than those in Q (Fig. 4.3b), which is in better agreement with the observed reflectivity fields (Fig. 4.3a). At 2-h forecast (valid at 0100 UTC), although the cells in region B are predicted in Q_qv at 1-h forecast (Fig. 4.3c), they are so weak and dissipate very quickly (Fig. 4.3f). Moreover, the intensity of the cell in region A at 1-h forecast in Q (Fig. 4.3b) decrease quickly and dissipate at 2-h forecast as well (Fig. 4.3e).

To quantitatively examine the performance of assimilating pseudo-water vapor observations, the equitable threat score (ETS, Clark et al., 2010) and bias (Roebber, 2009) are calculated where there are observations every hour for 0-3h forecasts from 2000 UTC to 2300 UTC with the thresholds of 20, 30 and 40 dBZ for experiments Q and Q_qv (Fig. 4.4). ETS = 0.0 indicates no skill of the prediction. The analysis or forecast is verified against reflectivity, which is better with the ETS increasing, and the best if ETS equals to 1.0. As for bias, the values close to 1.0 also represent good forecasts, or no bias. For the 20 dBZ thresholds (Fig. 4.4a), Q and Q_qv have nearly same ETS values at analysis time. However, Q_qv produces better skill for 1-3h forecasts compared to Q. For 30 and 40 dBZ thresholds (Figs. 4.4c, e), Q_qv has higher ETS values during all 0-3h forecast periods. Moreover, the biases for Q_qv are closer to 1.0 compared with those of Q. Overall, Q_qv has best forecast skills for all three thresholds which shows the assimilation of pseudo-water vapor is beneficial to the prediction.

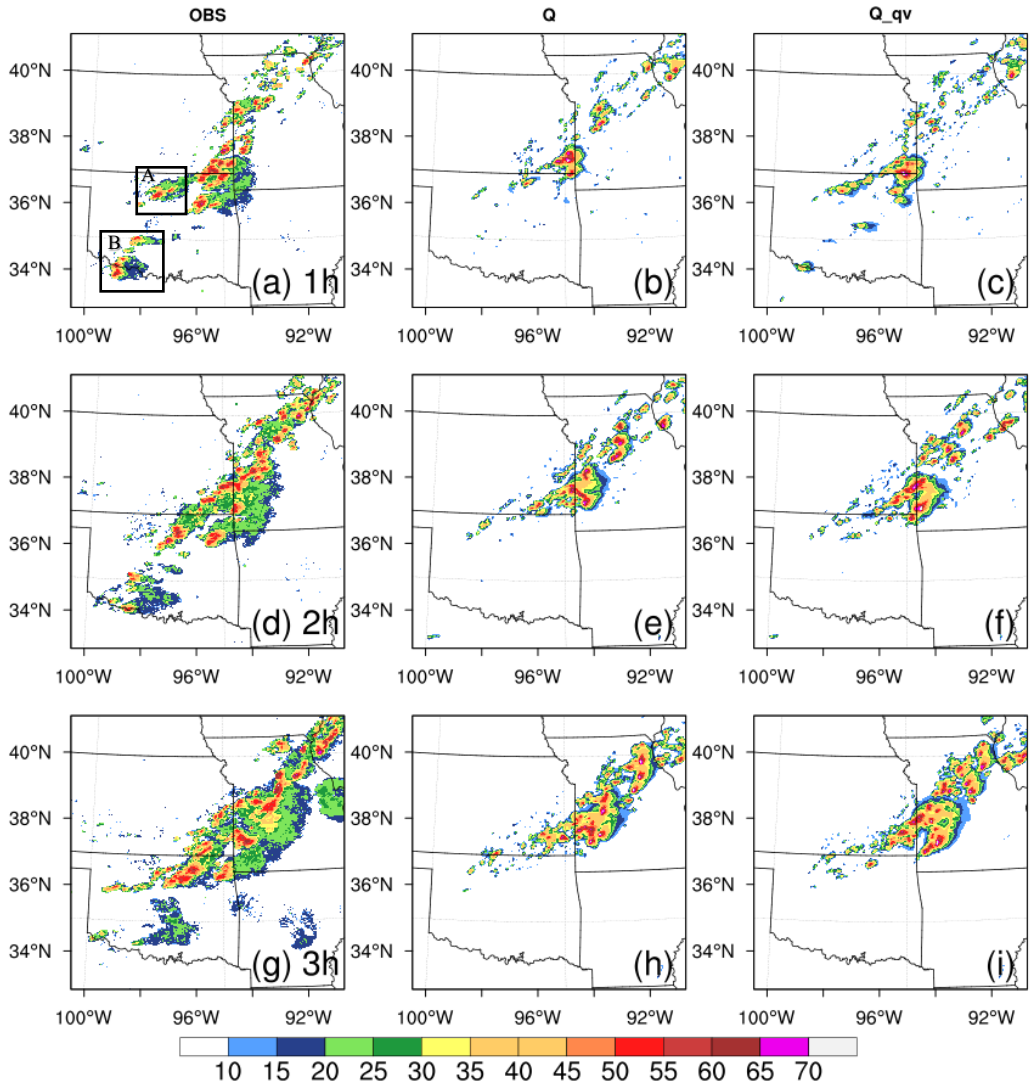

Figure 4.3: The observed composite reflectivity (left) and corresponding 1-3h forecasts initiated at 2300 UTC 22 May 2019 from experiments Q (middle) and Q_qv (right). Plots are shown for the 1-h forecast valid at 0000 UTC (a)-(c), 2-h forecast valid at 0100 UTC (d)-(f), 3-h forecast valid at 0200 UTC (g)-(i).

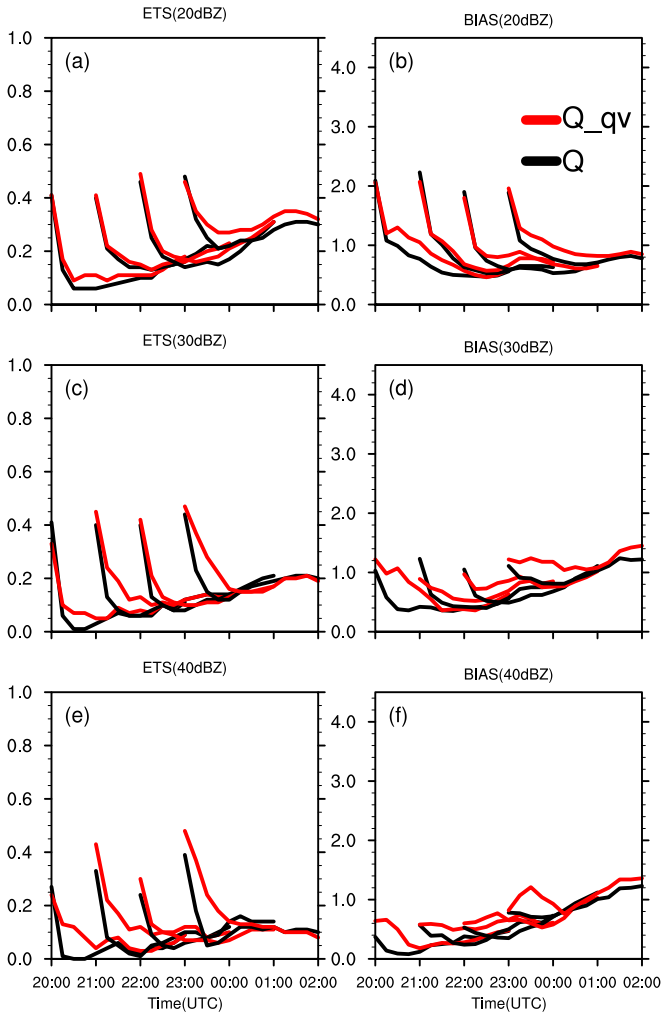

Figure 4.4: Equitable threat score (ETS) and bias of 0-3h forecasts for (a)-(b) 20 dBZ, (c)-(d) 30 dBZ and (e)-(f) 40 dBZ thresholds on 22 May 2019. The black lines are for experiment Q and the red lines are for experiment Q_qv.

4.1.2 **Results from comparison of experiments Q_qv, LOGQ_qv and PQ_qv**

As discussed above, the 0-3h forecasts from Q_qv are more consistent with the corresponding observed reflectivity fields when compared with Q. The experiment Q_qv obtains higher ETS values than Q indicating better forecast skills for Q_qv.

Because of the positive impact of assimilating pseudo-water vapor observations, they are also applied into all remaining experiments. In this section, three experiments Q_qv, LOGQ_qv and PQ_qv are compared to examine the impact of different transformation functions on the short-term forecasts. The analysis and forecast composite reflectivity fields from Q_qv, LOGQ_qv and PQ_qv for 0-3h forecasts initiated at 2300 UTC and corresponding observed composite reflectivity fields are shown in Fig. 4.5. The convective cells within the simulation domain are divided into three main regions (labeled as A, B and C) to better illustrate the comparisons. At the analysis time (valid at 2300 UTC), the reflectivity patterns of three experiments are similar to the observed composite reflectivity fields (Fig. 4.5a) in term of storm locations. However, the storm intensity differs from each experiment. The storm cells in region A from LOGQ_qv and PQ_qv (Figs. 4.5c, d) are stronger than that of Q_qv (Fig. 4.5b) and are more consistent with the observations. The analyzed reflectivity fields for LOGQ_qv (Fig. 4.5c) and PQ_qv (Fig. 4.5d) indicate that a cluster of several convective cells in region B is more vigorous than that for Q_qv (Fig. 4.5b), in better agreement with the observed reflectivity fields as well. Moreover, the weak cell in region C located in the southern boundary of the simulation domain for LOGQ_qv and PQ_qv is closer to the observations in terms of pattern and intensity.

Although using logarithmic and power transformed hydrometeor mixing ratios as control variables produces more consistent analyses of reflectivity fields, the performance does not persist in the forecasts. At 1-h forecast (0000 UTC), the left cells in region B and the weak cell in region C decay very quickly (Figs. 4.5f, g, h) and ultimately dissipate at 3-h forecast for all the three experiments (Figs. 4.5n, o, p).

To further evaluate the performance of different transformation functions applied on hydrometeor mixing ratios as control variables, the composite maximum reflectivity swaths for 0-3h forecasts initiated at 2300 UTC are compared with the observed composite reflectivity swaths (Fig. 4.6). The SPC storm reports are also overlaid in the simulation domain. From the forecast beginning at 2300 UTC, the forecasted reflectivity tracks are similar for all the experiments (Figs. 4.6b, c, d) but are all weaker than the observed reflectivity tracks (Fig. 4.6a). In addition, all three experiments miss the supercells in northeast Oklahoma which produced severe weather, including tornadoes and hail reports. For the storm cells in the border of Missouri and Illinois, there is a southward bias for all the experiments (Figs. 4.6b, c, d). The predicted reflectivity tracks over the boundary between Oklahoma and Missouri are more consistent with the observations for PQ_qv (Fig. 4.6d) with relatively smaller phase errors compared with that of Q_qv (Fig. 4.6b) and LOGQ_qv (Fig. 4.6c). Moreover, the mesoscale convective systems in north Missouri for LOGQ_qv and PQ_qv generate stronger forecasted composite reflectivity tracks than that of Q_qv.

In order to quantitatively investigate the performance of using logarithmic and power transformed mixing ratios as control variables, the ETS values are also calculated at every hour for 0-3h forecasts from 2000 UTC to 2300 UTC with the thresholds of 20,

30 and 40 dBZ for Q_qv, LOGQ_qv and PQ_qv (Fig. 4.7). At the analysis time, the ETS values for LOGQ_qv and PQ_qv are much higher than that for Q_qv for all thresholds which indicates that using logarithmic and power transformed mixing ratios as control variables greatly improves the analysis. Additionally, PQ_qv outperforms LOGQ_qv with higher ETS values at the analysis time. Although the logarithmic and power transformations of hydrometeor mixing ratios are beneficial for the analysis, their impact on the prediction is quite small. The ETS values for 0-3h forecast are quite similar for all three experiments which is consistent with the forecasted composite reflectivity fields.

The root-mean-square innovation (RMSI) is calculated in this study to quantify and compare the analysis performance of different transformation functions. The RMSIs of radar radial velocity and reflectivity analyses for the three experiments are shown in Fig. 4.8. For the RMSIs of radial velocity, LOGQ_qv and PQ_qv exhibit similar innovations which greatly reduces the errors associated with analyzed radial velocity when compared with Q_qv. Additionally, the forecast error growth is faster in Q_qv for radial velocity. For the RMSI of reflectivity, the innovations in analyzed reflectivity are smallest for PQ_qv and are largest for LOGQ_qv. Overall, PQ_qv has best performance with RMSIs in both radial velocity and reflectivity during the analysis cycles, suggesting that using power transformed mixing ratios as control variables produces most reasonable analyses.

As discussed above, PQ_qv produces higher ETS values than that of LOGQ_qv for all reflectivity thresholds at the analysis time. Also, although PQ_qv and LOGQ_qv exhibit very similar RMSIs for radial velocity, PQ_qv improves the analyzed reflectivity with the smallest RMSIs during the analysis cycles. To further simplify the comparison,

only Q_qv and PQ_qv are considered in the rest of section to thoroughly examine the impact of assimilating the power transformed control variables.

To compare the convergence rates of Q_qv and PQ_qv, the cost functions of total and individual observational parts (radial velocity, reflectivity and pseudo-water vapor) normalized by their corresponding initial values are calculated (Fig. 4.9). It is suggested that PQ_qv has faster convergence rates than Q_qv, especially for radial velocity and pseudo-water vapor observations (Figs. 4.9b, d). For the cost functions of total and reflectivity (Figs. 4.9a, c), Q_qv and PQ_qv exhibit very similar convergence rates.

To quantitatively evaluate the prediction skill for precipitation by using different control variables, the fractions skill scores (FSS, Roberts & Lean, 2008) of 1-h accumulated precipitation for Q_qv and PQ_qv with different thresholds are calculated (Fig. 4.10). The precipitation forecasts are verified against National Centers for Environmental Prediction (NCEP) Stage IV precipitation dataset (Y. Lin, 2011). For the 0-1h forecast (Fig. 4.10a), PQ_qv has relatively higher score for all thresholds than that of Q_qv. For the 1-2h forecast (Fig. 4.10b), Q_qv and PQ_qv show similar FSS values at the threshold of 1mm. PQ_qv outperforms Q_qv for higher scores at the thresholds of 2.5mm and 5mm. For the 2-3h forecast (Fig. 4.10c), the FSSs of PQ_qv are slightly higher than that of Q_qv for 2.5mm and 5mm thresholds. However, Q_qv produces higher scores at the threshold of 10mm. Overall, using power transformed hydrometeor mixing ratios as control variables exhibits better quantitative precipitation prediction forecast (QPF) skills.

The performance diagrams (Roebber, 2009) are analyzed in this section to supply a thorough examination of the overall performance of the analysis and forecast by using

different control variables. The probability of detection (POD), bias, critical success index (CSI) and false alarm ratio (FAR) or its equivalent, success ratio (SR = 1 - FAR) are all included in the performance diagrams. Fig. 4.11 shows the performance diagrams for 0-3h forecasts initiated at 2300 UTC with 20, 30 and 40 dBZ thresholds. The closer the values of POD, CSI and SR are to unity, the better the forecast is. Therefore, the upper right of the diagram indicates a perfect forecast. At the analysis time, although the POD value of PQ_qv is slightly lower than that of Q_qv at the threshold of 20 dBZ (Fig. 4.11a), PQ_qv produces higher CSI and SR for reflectivity at all thresholds indicating the improvement of analysis in PQ_qv. At 1-h forecast, Q_qv performs better than PQ_qv. As for 2-3h forecasts, Q_qv and PQ_qv exhibit similar performance which is in agreement with the evaluation with ETS.

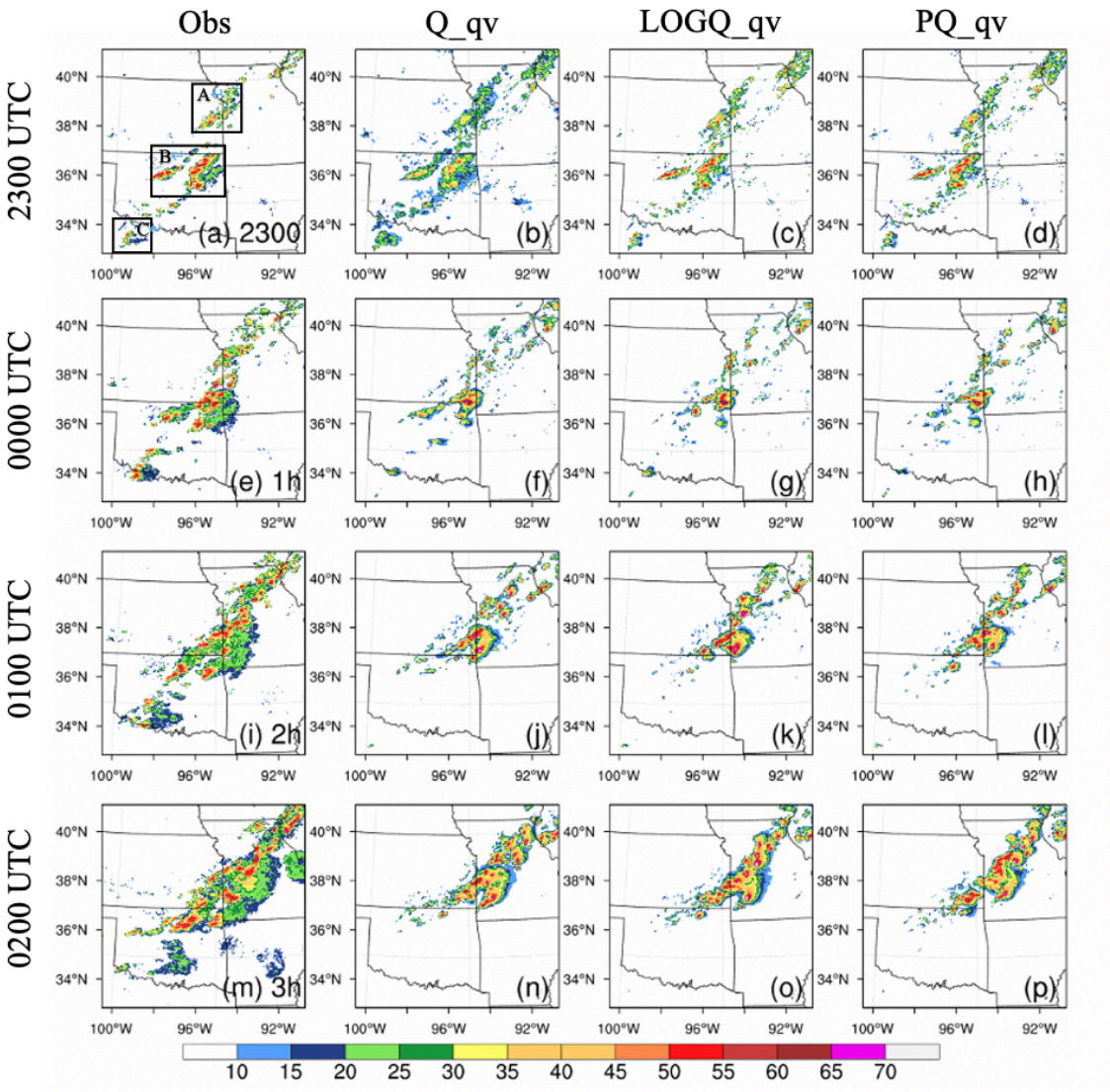

Figure 4.5: The observed composite reflectivity (left) and corresponding 0-3h forecasts initiated at 2300 UTC 22 May 2019 from experiments Q_qv (second column), LOGQ_qv (third column) and PQ_qv (right). Plots are shown for the analysis time at 2300 UTC (a)-(d), the 1-h forecast valid at 0000 UTC (e)-(h), 2-h forecast valid at 0100 UTC (i)-(l), 3-h forecast valid at 0200 UTC (m)-(p).

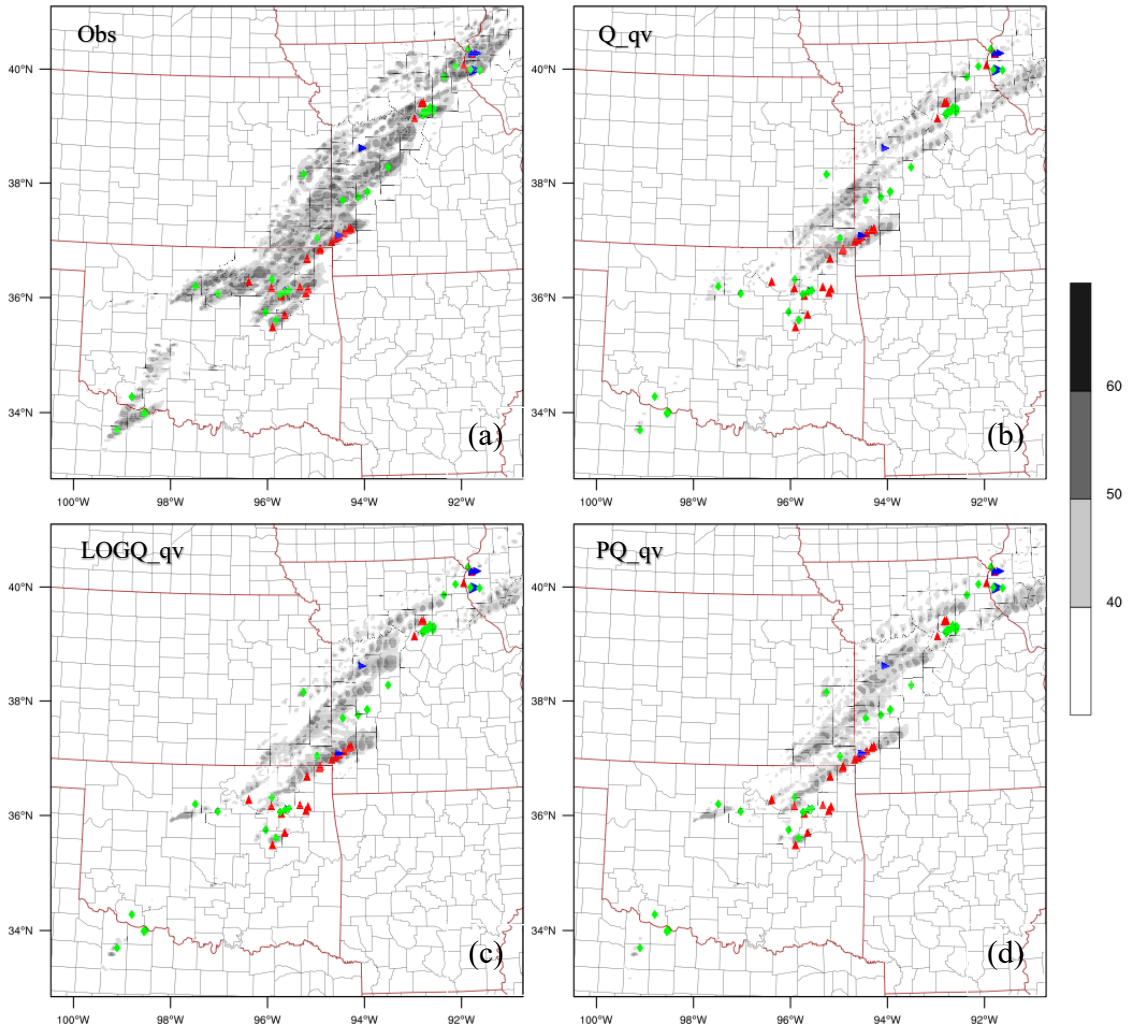

Figure 4.6: Composite maximum reflectivity swaths: observed (a), Q_qv (b), LOGQ_qv (c) and PQ_qv (d) for 0-3h forecasts initiated at 2300 UTC 22 May 2019. The green rhombuses, red and blue triangles represent hail, tornadoes and damaging winds from SPC reports, respectively.

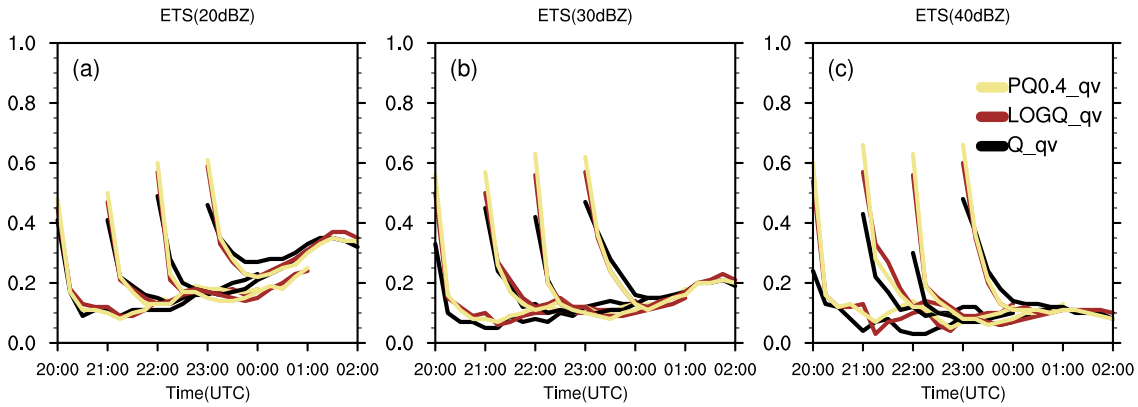

Figure 4.7: Equitable threat score (ETS) of 0-3h forecasts for 20 dBZ (a), 30 dBZ (b) and 40 dBZ (c) thresholds on 22 May 2019. The black, brown and khaki lines represent Q_qv, LOGQ_qv and PQ_qv forecasts, respectively.

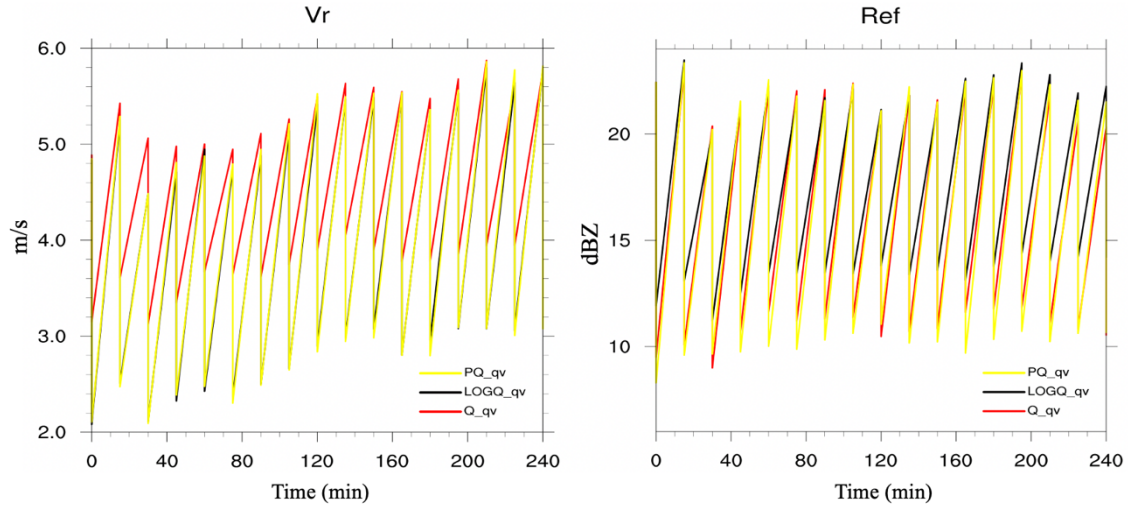

Figure 4.8: The RMSIs of (left) radial velocity (m/s) and (right) reflectivity (dBZ) analyses from Q_qv (red line), LOGQ_qv (black line) and PQ_qv (yellow line).

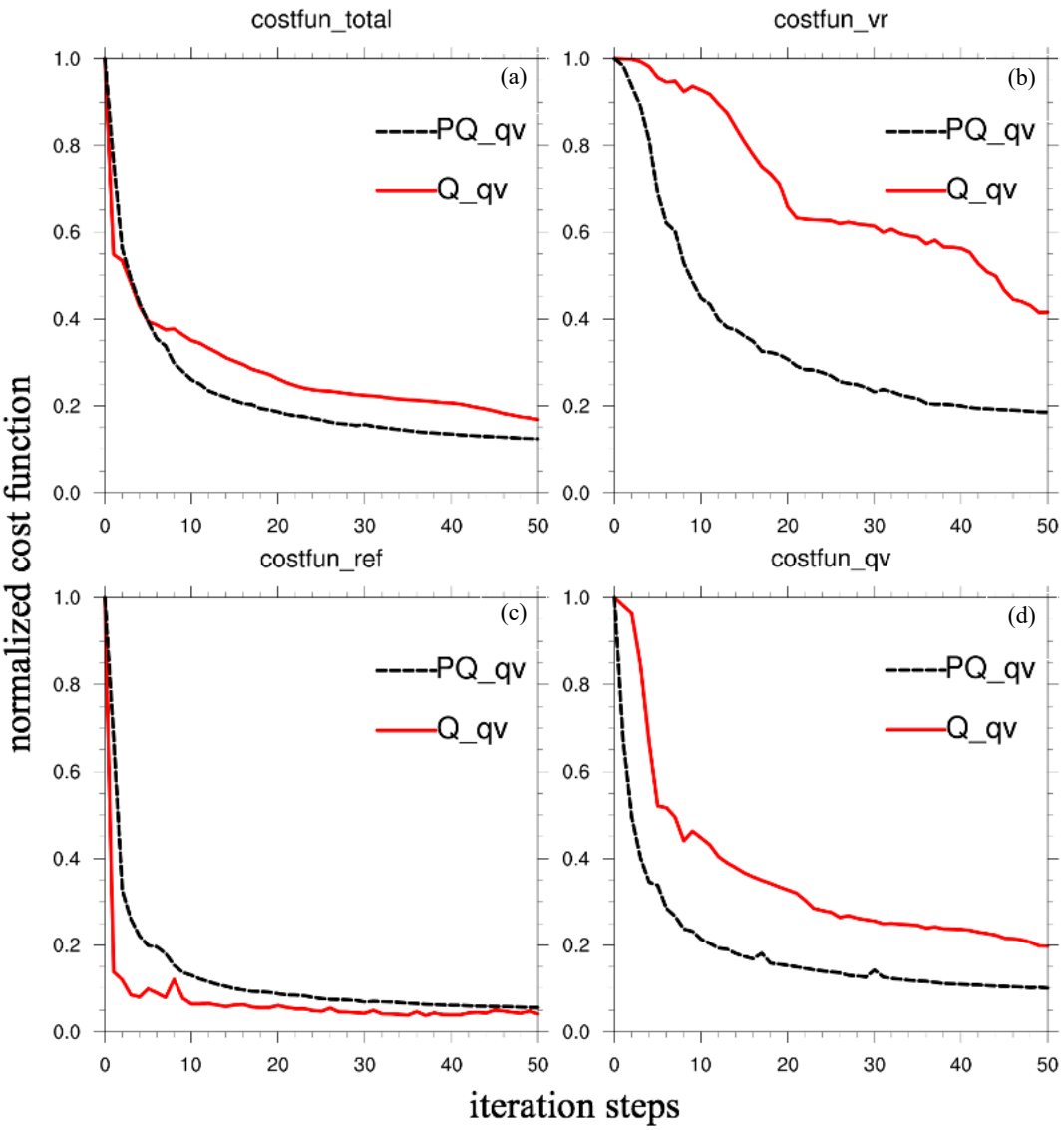

Figure 4.9: The normalized cost function of total (a), radial velocity (b), reflectivity (c) and pseudo-water vapor (d) for Q_qv and PQ_qv for the analysis at 1900 UTC 22 May 2019.

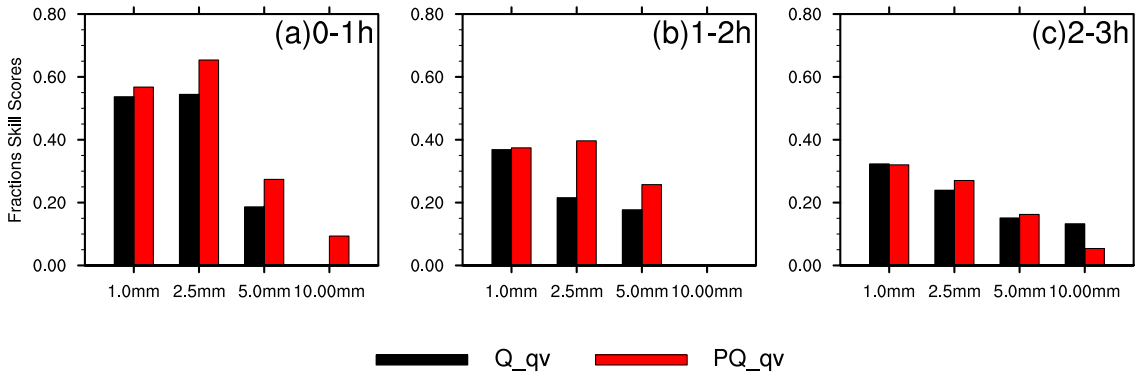

Figure 4.10: The FSSs of 1-h accumulated precipitation with different thresholds for Q_qv and PQ_qv.

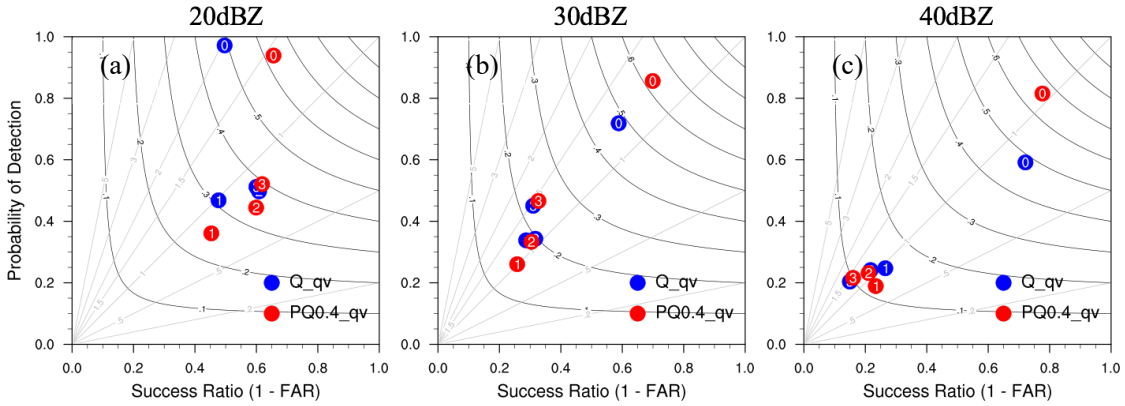

Figure 4.11: Performance diagrams for 0-3h forecasts of composite reflectivity fields beginning at 2300 UTC 22 May 2019 for 20dBZ (a), 30dBZ (b) and 40 dBZ (c) thresholds. The black curves represent the critical success index (CSI) and the diagonal gray lines represent the bias. The number in the dots is the forecast length ("0" represents 0-h forecast or analysis, "1" represents 1-h forecast … etc.).

4.1.3 **Results from comparison of experiments PQ_qv with PQ_Pqv**

As described earlier, the assimilation of pseudo-water vapor observations along with radar radial velocity and reflectivity has positive impact on the analyses and forecasts of convective storms. Moreover, using power transformed mixing ratios as control variables greatly improves the analyses and has faster convergence rates. Therefore, the power transformation function is also applied on pseudo-water vapor in this section to test whether it can help improve convective scale short term severe weather forecasts.

The performance diagrams for 0-3h forecasts initiated at 2200 UTC and 2300 UTC for PQ_qv and PQ_Pqv are compared (Fig. 4.12). At the analysis time, the impact of applying power transformation function on pseudo-water vapor is mixed. PQ_Pqv produces slightly lower CSI and SR values than that of PQ_qv for all thresholds. Additionally, these discrepancies between the experiments increase with the reflectivity threshold from 20 dBZ to 40 dBZ. For the 1-3h forecasts, the POD and SR values of PQ_Pqv are higher at all thresholds along with an increase in CSI, especially for 2h and 3h forecast. This indicates that using power transformed pseudo-water vapor as control variables is slightly beneficial for short term forecasts.

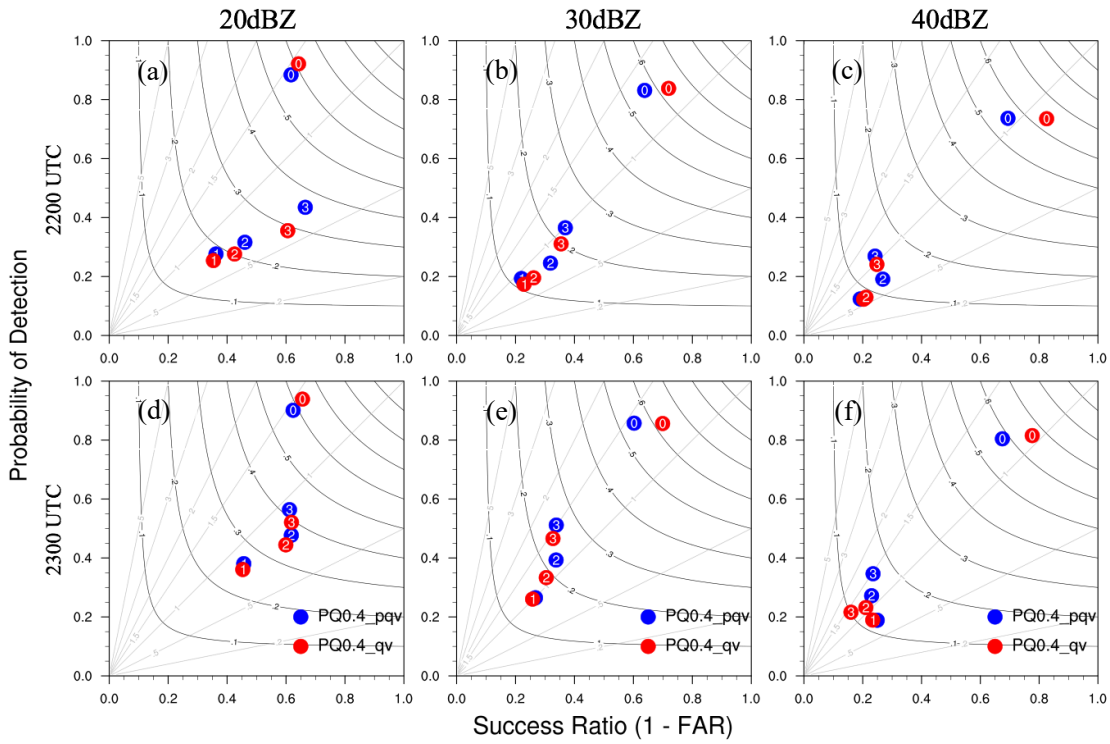

Figure 4.12: As in Fig. 4.11, but for PQ_qv and PQ_Pqv and it is initiated at 2200 UTC and 2300 UTC.

4.2 Overview of the 28 May 2019 case

The second case selected for this study occurred on May 28, 2019. Initially in the afternoon that day, there was a slow-moving front from northeastern Kansas into northern Missouri. Storms formed and moved northeastward along the front. Scattered supercells developed along the dryline from west central Oklahoma northward into central Kansas which favored the development of very large hail (3 inches in diameter likely). The ongoing elevated thunderstorms persisted for several hours and isolated severe storms formed and moved eastward across west central Kansas through the evening. These storms produced several tornadoes. Eventually, an EF4 tornado formed with maximum winds of 170 mph. In all, 35 tornadoes were reported ranging from EF0 to EF4, and among them 21 tornadoes occurred in Kansas.

The simulation domain of the experiments for 28 May 2019 case includes most of Oklahoma, Kansas, Missouri, Arkansas, Iowa and Illinois (Figs. 4.13, 4.14).

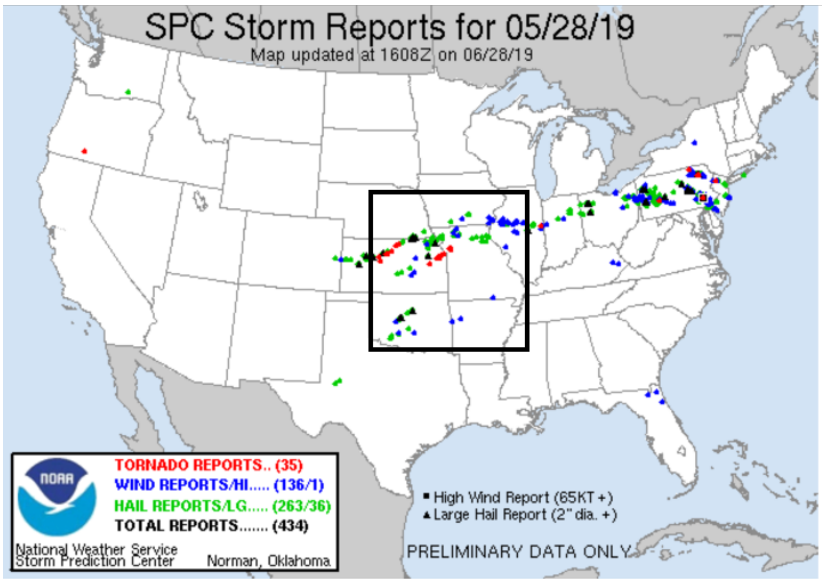

Figure 4.13: As in Fig. 4.1, except for 28 May 2019.

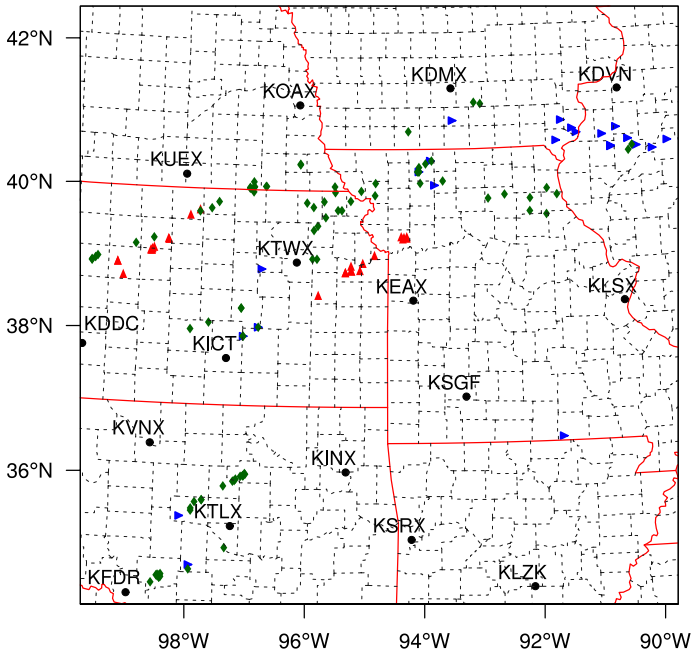

Figure 4.14: As in Fig. 4.2, except for 28 May 2019. The geographical center of the model simulation domain is at (38.42N, 94.75W).

4.2.1 **Results from comparison of experiments Q with Q_qv**

First of all, we compare the experiments Q with Q_qv to investigate the impact of assimilating pseudo-water vapor observations along with radar radial velocity and reflectivity. The forecasted composite reflectivity fields from experiments Q and Q_qv for 1-3 h forecasts initiated at 2200 UTC are compared with observed composite reflectivity (Fig. 4.15). Similar to the last case, to better illustrate the differences between two experiments compared with the observations, three main regions are marked and labeled as A, B and C from north to south in the simulation domain (Fig. 4.15a). The observed composite reflectivity fields show that the weak cells in south central Kansas at 2300 UTC (Fig. 4.15a) grow quickly which merge with the convective cells in region A to form a MCS at 0100 UTC (Fig. 4.15g). There are two major supercells in region C which gradually move northeastward. Additionally, several storm cells in the east border of Kansas and Missouri gradually weaken while propagating eastward.

At 1-h forecast (valid at 2300 UTC), the convective cells in region A which is located in the northwest of Kansas dissipate in the experiment Q (Fig. 4.15b) but are predicted in Q_qv (Fig. 4.15c) though with smaller coverage. In addition, a weak cell in region B is predicted in Q_qv but not in Q. At 2-h forecast (valid at 0000 UTC), although the weak cell in region B is well predicted in Q_qv, it weakened very quickly and completely dissipated (Fig. 4.15f). Moreover, the southernmost cell in region C is not predicted in Q (Figs. 4.15b, e), but intensifies in Q_qv (Figs. 4.15c, f) which is more consistent with the corresponding observations (Figs. 4.15a, d).

To quantitatively examine the performance of assimilating pseudo-water vapor observations, the ETS and bias are calculated at every hour for 0-3h forecasts from 2000

UTC to 2300 UTC with the thresholds of 20, 30 and 40 dBZ in experiments Q and Q_qv (Fig. 4.16). For the threshold of 20 dBZ, Q_qv has higher ETS values than that of Q during the entire 0-3h forecasts (Fig. 4.16a). For the 30 and 40 dBZ thresholds, Q_qv greatly improves the analysis for higher ETS values (Figs. 4.16c, e). However, Q_qv shows only slightly better prediction skills 2-h into the forecasts. As for bias, the value of Q_qv is closer to 1.0 indicating better forecasts with little biases, especially for the thresholds of 20 and 30 dBZ (Figs. 4.16b, d). Overall, Q_qv has better forecast skills for all the thresholds which shows the assimilation of pseudo-water vapor is beneficial to the convective scale short-term forecasts.

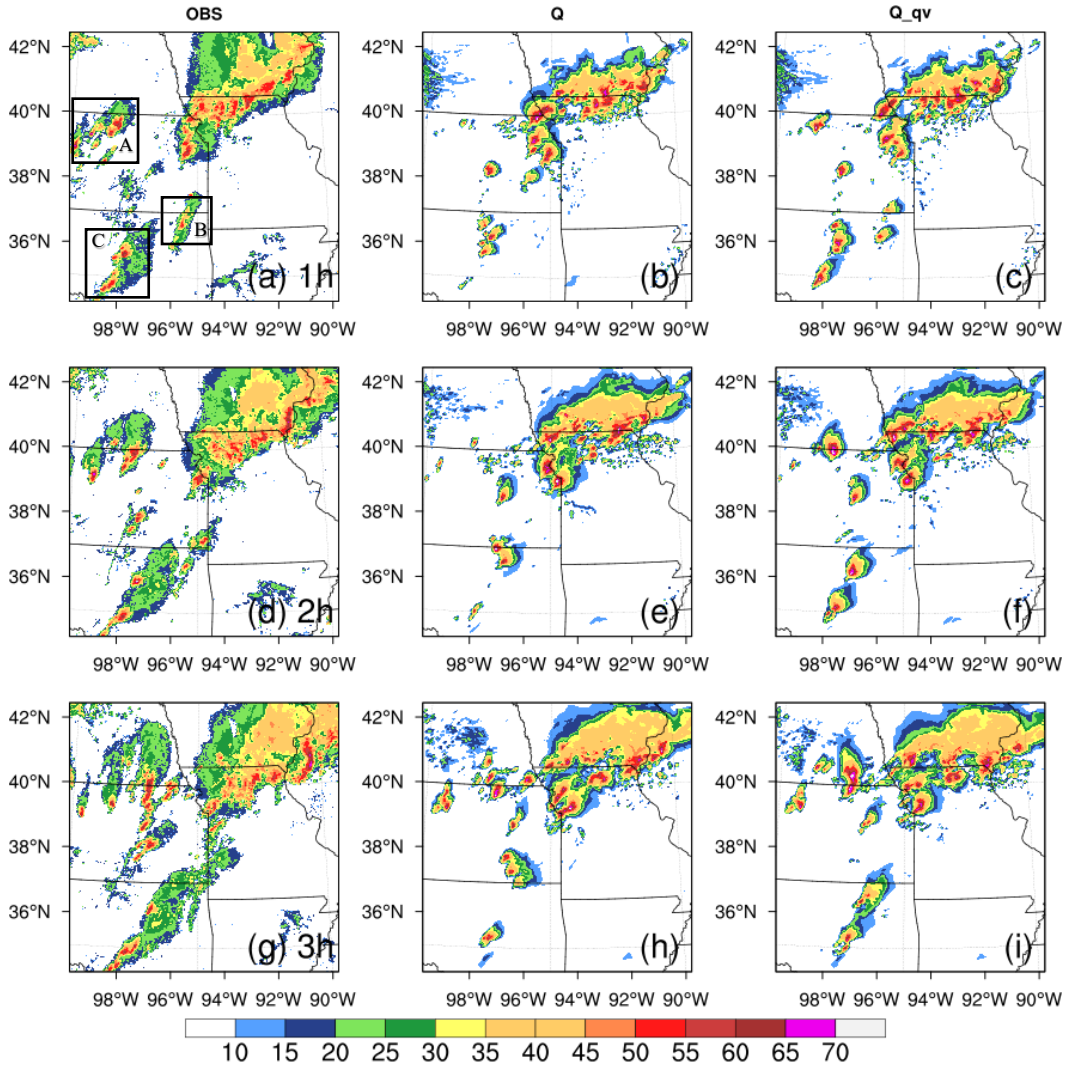

Figure 4.15: As in Fig. 4.3, except for 28 May 2019 and it is initiated at 2200 UTC.

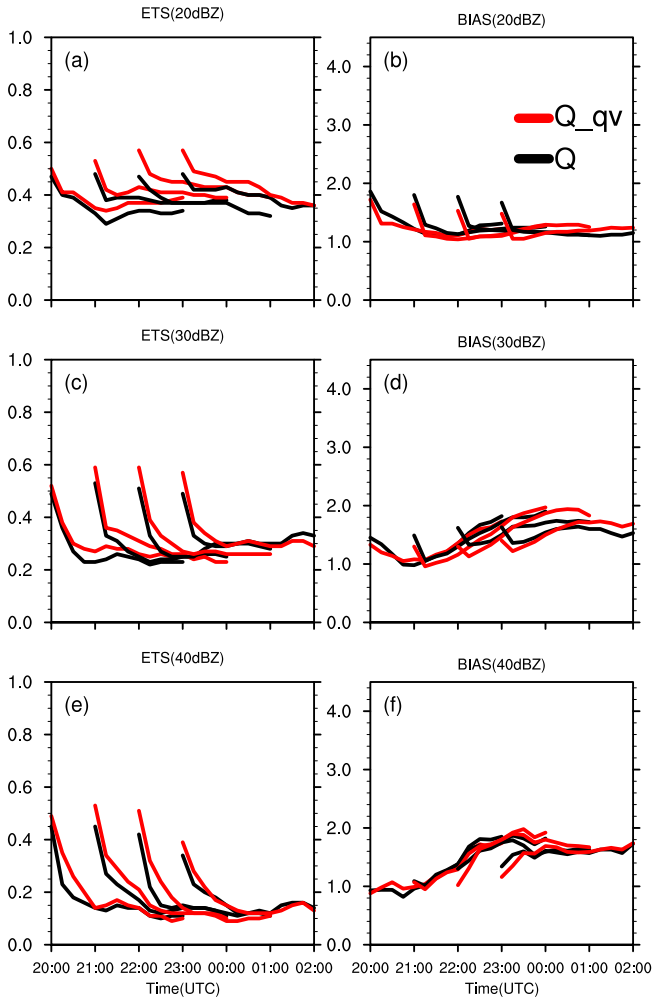

Figure 4.16: As in Fig. 4.4, except for 28 May 2019.

4.2.2 **Results from comparison of experiments Q_qv, LOGQ_qv and PQ_qv**

Similar to the first case, three experiments Q_qv, LOGQ_qv and PQ_qv are compared to examine the usefulness of different transformation functions. The analyzed and forecasted composite reflectivity fields for 0-3h forecasts initiated at 2200 UTC for the three experiments Q_qv, LOGQ_qv and PQ_qv and corresponding observed composite reflectivity fields are shown in Fig. 4.17. The three main regions from north to south are marked and labeled as A, B and C to better illustrate the comparisons. At the analysis time (valid at 2200 UTC), the reflectivity patterns of three experiments are similar to the observed composite reflectivity (Fig. 4.17a) in term of storm locations. Similar to the first case, however, the storm intensity differs from each experiment. The intensity of the cell in region A for LOGQ_qv and PQ_qv (Figs. 4.17c, d) is closer to the observations compared with that of Q_qv (Fig. 4.17b). The analyzed reflectivity fields for LOGQ_qv (Fig. 4.17c) and PQ_qv (Fig. 4.17d) indicate that the convective cells in region B for both experiments are more vigorous than that for Q_qv (Fig. 4.17b), in better agreement with the observed reflectivity fields. Moreover, a cluster of several storm cells in region C from LOGQ_qv and PQ_qv are also stronger in comparison with Q_qv which shows more consistence with the observations. Spurious cells are produced in Q_qv, especially in south Nebraska and the border of Oklahoma and Kansas, which can be greatly reduced in both LOGQ_qv and PQ_qv.

Although using logarithmic and power transformed hydrometeor mixing ratios as control variables produces more consistent analyses of reflectivity fields, the performance cannot persist in the forecasts. At 1-h forecast (valid at 2300 UTC), there are several convective cells in region A for both LOGQ_qv and PQ_qv (Figs. 4.17g, h), while only

one cell in Q_qv (Fig. 4.17f). However, other cells dissipate when moving northward in LOGQ_qv and PQ_qv at 2-h forecast (Figs. 4.17k, l). At 3-h forecast, there is a spurious cell in southern Kansas for LOGQ_qv (Fig. 4.17o) while PQ_qv can alleviate this issue (Fig. 4.17p), which is consistent with the findings in previous studies (Carley, 2012; Chen et al., 2020; Liu et al., 2020). Totally, all the three experiments exhibit very similar forecast performance for composite reflectivity fields.

To further evaluate the performance of different transformation functions applied to hydrometeor mixing ratios as control variables, the composite maximum reflectivity swaths for 0-3h forecasts initiated at 2200 UTC are compared with the observed reflectivity swaths (Fig. 4.18). From the forecast beginning at 2200 UTC, the reflectivity tracks are similar for all the experiments (Figs. 4.18b, c, d) but are all weaker than the observed reflectivity tracks (Fig. 4.18a). In addition, the three experiments all exhibit a clear northward bias, especially for the storm tracks in central and north of Oklahoma, central Kansas and the border between Kansas and Nebraska. However, there still exists a few discrepancies among the three experiments. The predicted reflectivity tracks over the boundary between Kansas and Missouri where the tornadoes are observed are more consistent with the observations for PQ_qv (Fig. 4.18d) and LOGQ_qv (Fig. 4.18c) with smaller phase errors and stronger intensities compared with that of Q_qv (Fig. 4.18b).

The ETS values are calculated at every hour for 0-3h forecasts from 2000 UTC to 2300 UTC with the thresholds of 20, 30 and 40 dBZ for all three experiments Q_qv, LOGQ_qv and PQ_qv to quantitatively investigate the performance (Fig. 4.19). At the analysis time, the ETS values for LOGQ_qv and PQ_qv are much higher than that for Q_qv for all thresholds which indicates that using logarithmic and power transformed

mixing ratios as control variables greatly improves the analyses. Additionally, PQ_qv outperforms LOGQ_qv with higher ETS values, especially at the analysis time. However, the contributions from LOGQ_qv and PQ_qv to the prediction are mixed. For the 20 dBZ threshold (Fig. 4.19a), the ETS for Q_qv is superior at 1-h forecast. For the thresholds of 30 and 40 dBZ (Figs. 4.19b, c), the three experiments have very similar ETS values at 2-3h forecasts.

The RMSIs of radar radial velocity and reflectivity analyses for the three experiments are shown in Fig. 4.20. For the RMSI of radial velocity, LOGQ_qv and PQ_qv exhibit similar innovations which greatly reduce the errors associated with analyzed radial velocity compared with Q_qv. For the RMSI of reflectivity, the innovations in analyzed reflectivity are smallest for each cycle with PQ_qv. However, the forecast error growth is faster in LOGQ_qv and PQ_qv than that in Q_qv for reflectivity. Similar to the first case, PQ_qv produces more balanced analyses for lower RMSI values in both radial velocity and reflectivity.

Since PQ_qv produces higher ETS values than that of LOGQ_qv for all reflectivity thresholds at the analysis time and improves the analyzed reflectivity with the smallest RMSIs during the analysis cycles, only Q_qv and PQ_qv are compared with the convergence rates to thoroughly examine the impact of the use of the transformed control variables. The cost functions of total and individual parts are presented (Fig. 4.21). It is shown that PQ_qv has faster convergence rates than Q_qv, especially for the parts corresponding to radial velocity and pseudo-water vapor (Figs. 4.21b, d). For the normalized total cost function (Fig. 4.21a), Q_qv converges faster at the first two iteration steps and PQ_qv converges faster for the rest of iterations. For the reflectivity (Fig. 4.21c),

Q_qv has faster convergence rates at the first six iteration steps. Overall, PQ_qv converges faster by reaching the smallest cost function values in comparison with that of Q_qv.

To quantitatively evaluate the QPF skills by using different control variables, the FSSs of 1-h accumulated precipitation for Q_qv and PQ_qv with different thresholds are calculated (Fig. 4.22). When the threshold increases from 1.0 mm to 10.0 mm, the scores decrease for both Q_qv and PQ_qv. For the 0-1h forecast (Fig. 4.22a), PQ_qv has relatively higher FSS values for all thresholds when compared with Q_qv. For the 1-2h and 2-3h forecasts (Figs. 4.22b, c), Q_qv and PQ_qv produce similar FSS values. However, the FSSs of PQ_qv are slightly lower than that of Q_qv, especially at 5.0mm and 10.0mm thresholds.

Fig. 4.23 shows the performance diagrams for 0-3h forecasts initiated at 2200 UTC with 20, 30 and 40 dBZ thresholds. At the analysis time, although the POD value of PQ_qv is slightly lower than that of Q_qv at the threshold of 20 dBZ (Fig. 4.23a), PQ_qv produces higher CSI and SR for reflectivity at all thresholds indicating the improvement of analysis in PQ_qv. As for 1-3h forecasts, Q_qv and PQ_qv exhibit similar performance at 30 dBZ threshold. For the thresholds of 20 and 40 dBZ, PQ_qv performs better for slightly higher SR values, especially for 1-h forecast.

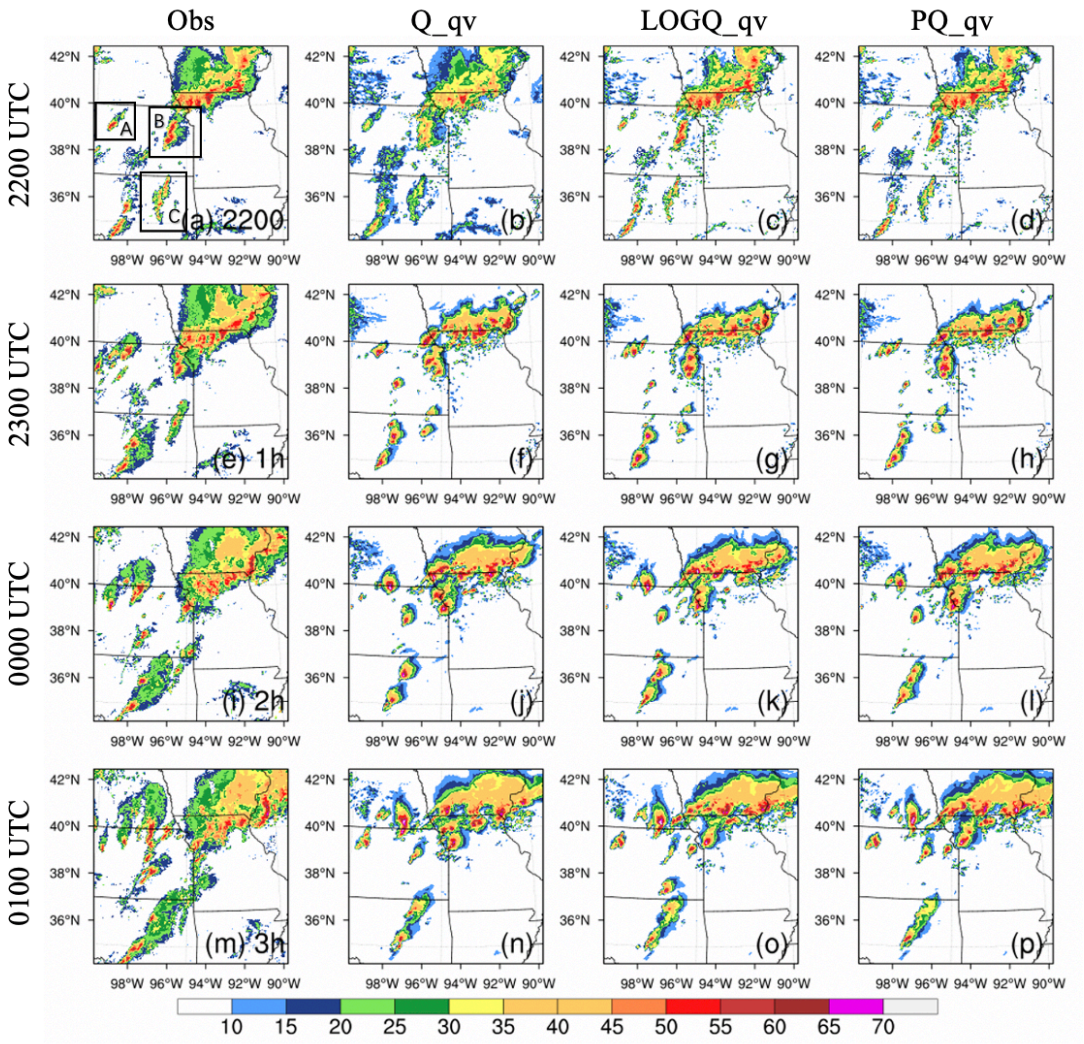

Figure 4.17: As in Fig. 4.5, except for 28 May 2019 and it is initiated at 2200 UTC.

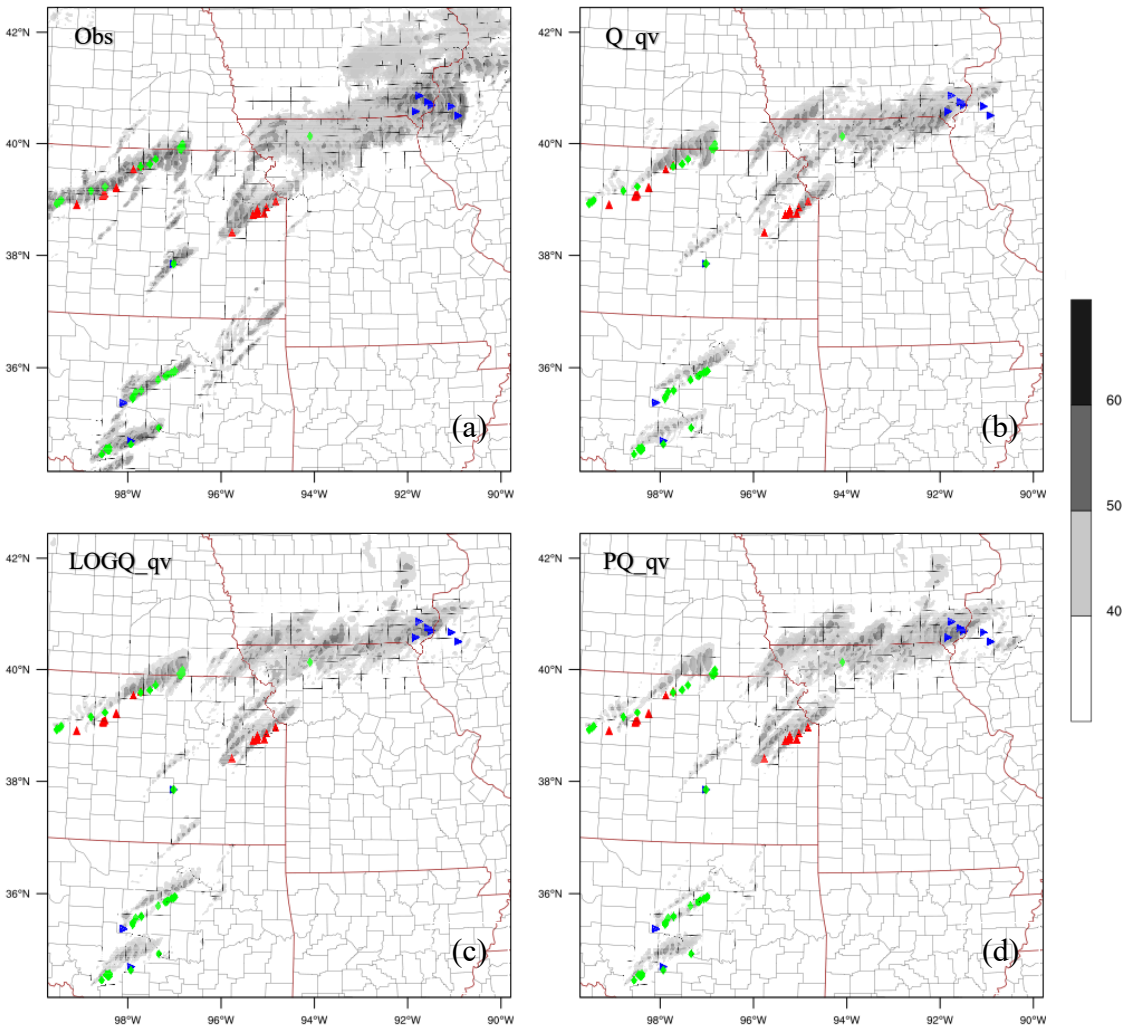

Figure 4.18: As in Fig. 4.6, except for 28 May 2019 and it is initiated at 2200 UTC.

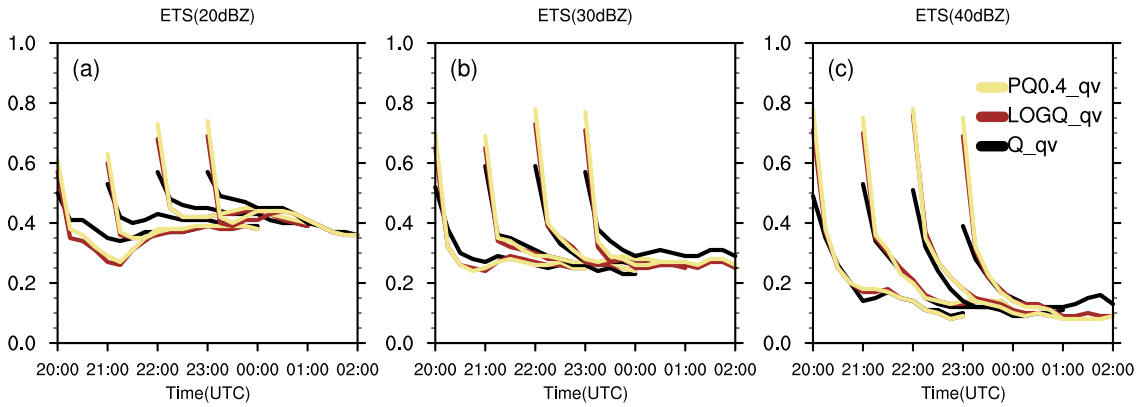

Figure 4.19: As in Fig. 4.7, except for 28 May 2019.

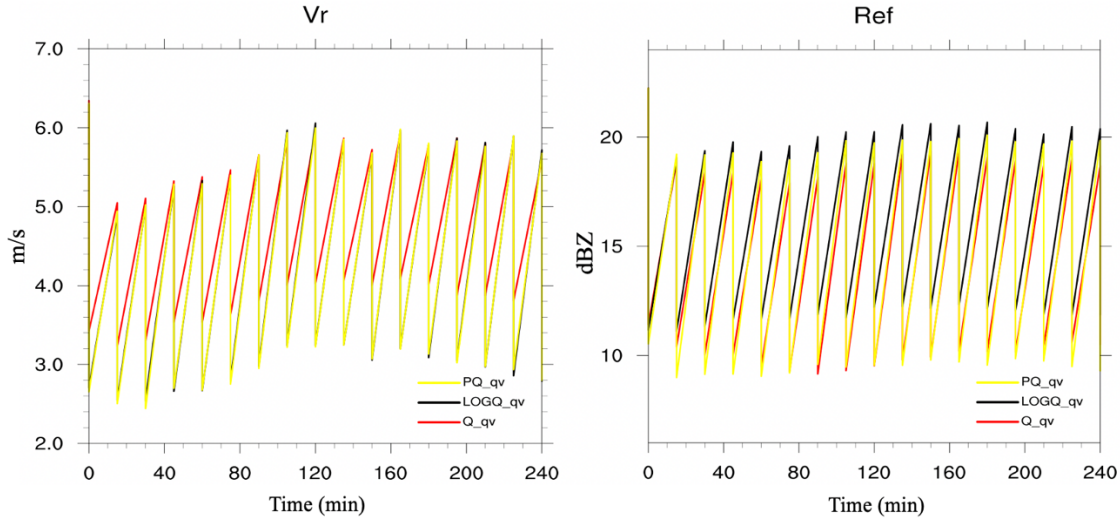

Figure 4.20: As in Fig. 4.8, except for 28 May 2019.

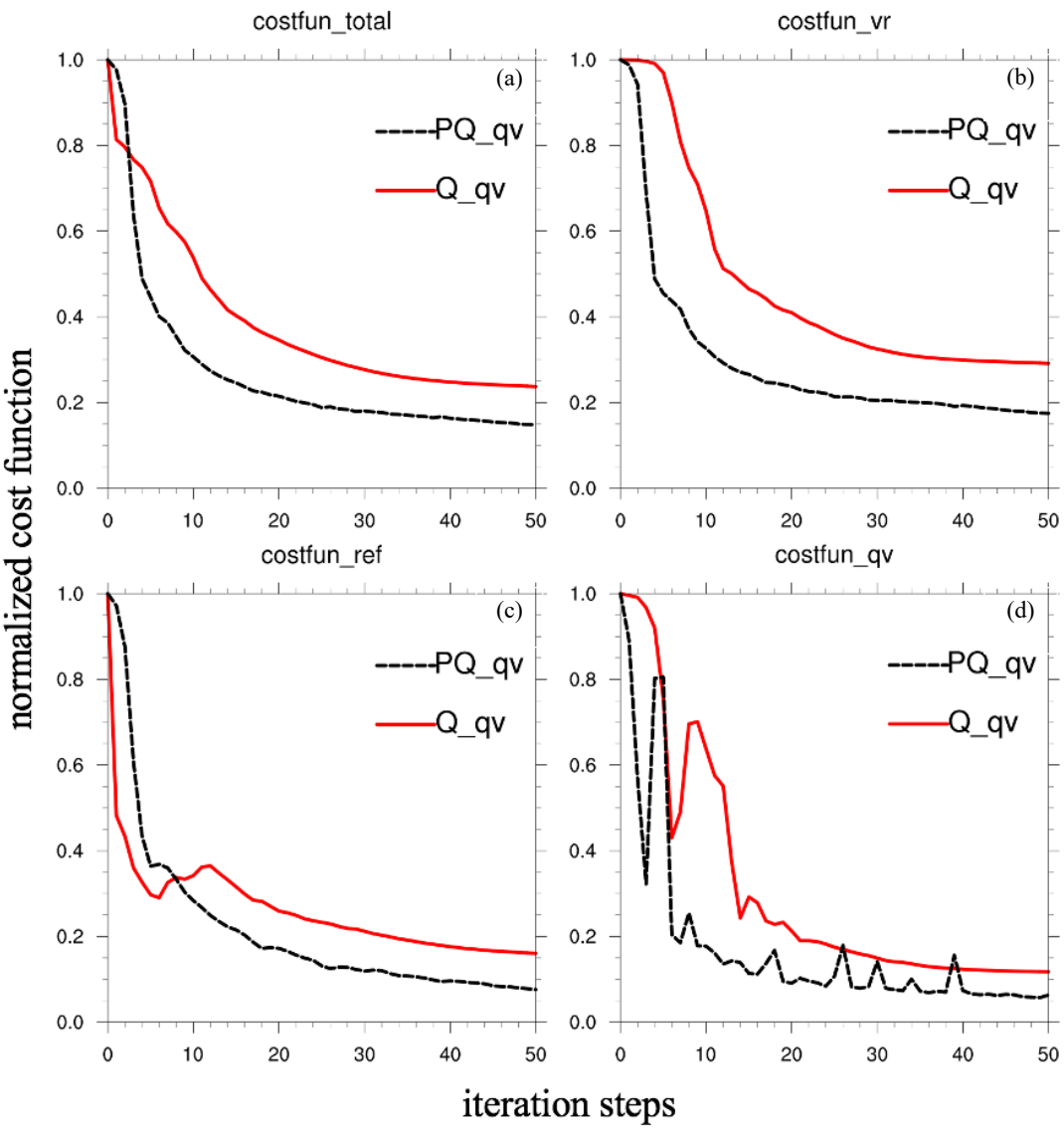

Figure 4.21: As in Fig. 4.9, except for 28 May 2019.

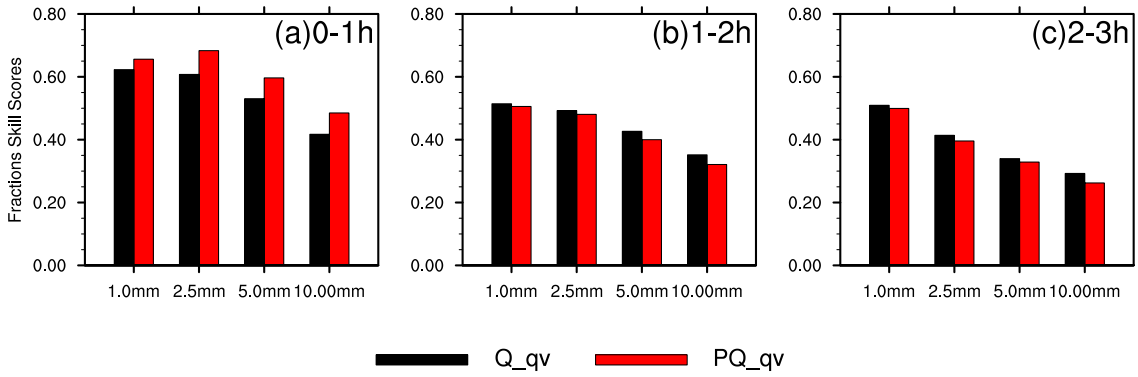

Figure 4.22: As in Fig. 4.10, except for 28 May 2019.

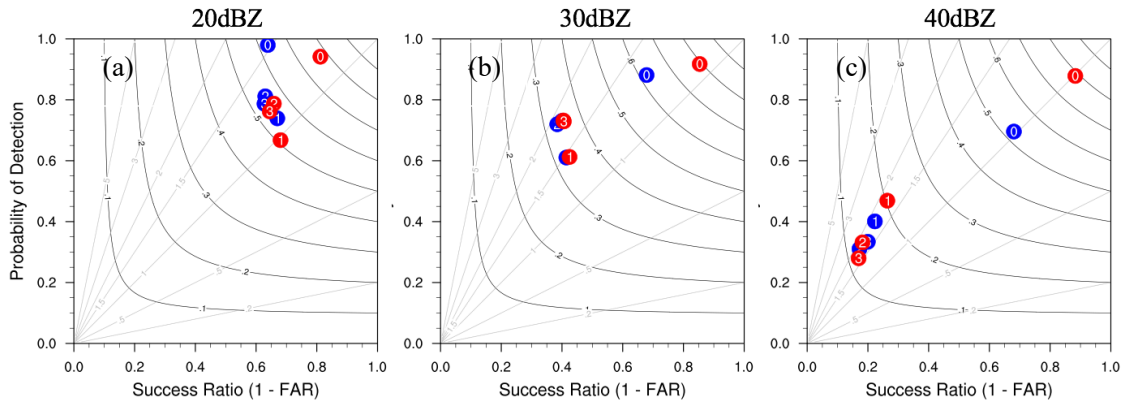

Figure 4.23: As in Fig. 4.11, except for 28 May 2019 and it is initiated at 2200 UTC. The red and blue dots represent PQ_qv and Q_qv, respectively.

4.2.3 **Results from comparison of experiments PQ_qv with PQ_Pqv**

The power transformation functions are also applied on pseudo-water vapor observations for this case. The performance diagrams for 0-3 h forecasts initiated at 2200 UTC and 2300 UTC for PQ_qv and PQ_Pqv are shown (Fig. 4.24) to test whether PQ_Pqv can help improve convective scale short term severe weather forecasts.

At the analysis time (0-h forecast), the impact of applying power transformation function on pseudo-water vapor is little bit better. PQ_Pqv produces slightly lower CSI and SR values than that of PQ_qv for all thresholds. As for 1-3h forecasts, PQ_qv and PQ_Pqv show very similar performance. The POD of PQ_Pqv is slightly higher than that of PQ_qv at 1-h forecast.

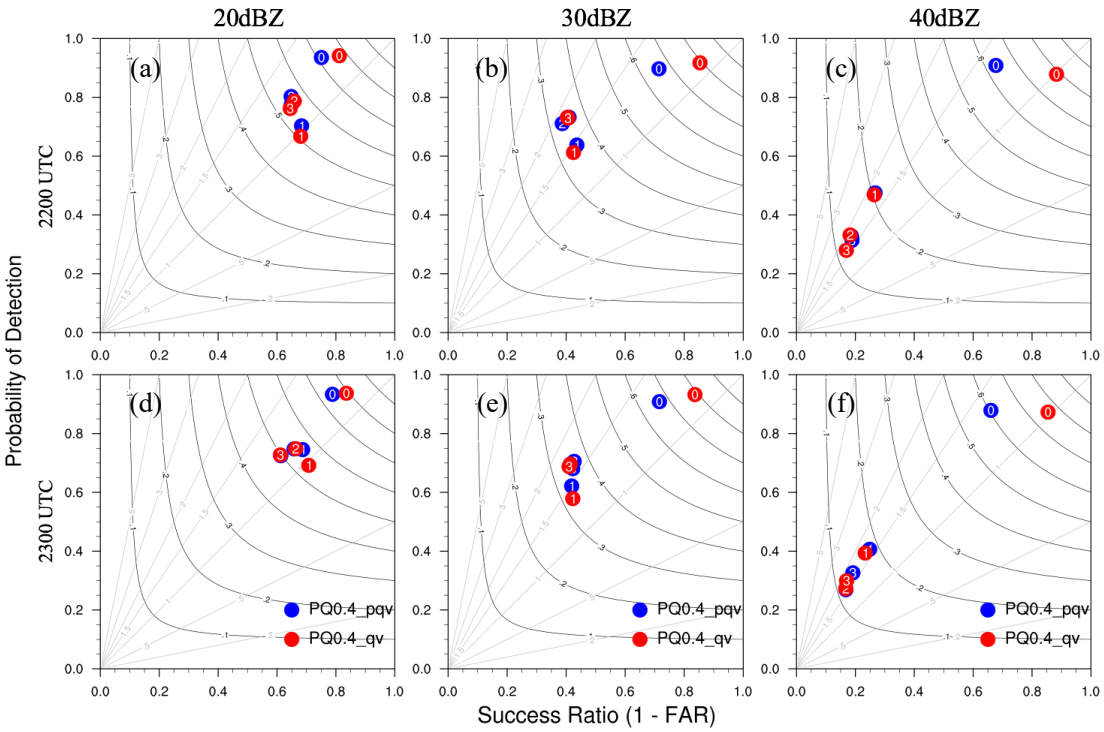

Figure 4.24: As in Fig. 4.12, except for 28 May 2019.

4.3 Overview of the 20 May 2019 case

The third case selected for this study occurred on May 20, 2019. Early in the afternoon, several supercell thunderstorms developed across west Texas, the eastern half of the Texas Panhandle. These thunderstorms produced an outbreak of tornadoes which included intense and long-track tornadoes and very large hail events (4 inches in diameter). In the early evening, semi-discrete storms from far eastern Oklahoma evolved and produced tornadoes as they gradually moved northeastward across northeast Oklahoma, southwest Missouri and southeast Kansas. In the late evening, the isolated supercells persisted across the Low Rolling Plains with more storms initiated farther across southwest Texas. In all, 38 tornadoes were reported ranging from EF0 to EF1 and 17 of them occurred in Oklahoma.

The simulation domain of the experiments for 20 May 2019 case includes most of Texas, Oklahoma and Kansas (Figs. 4.25, 4.26).

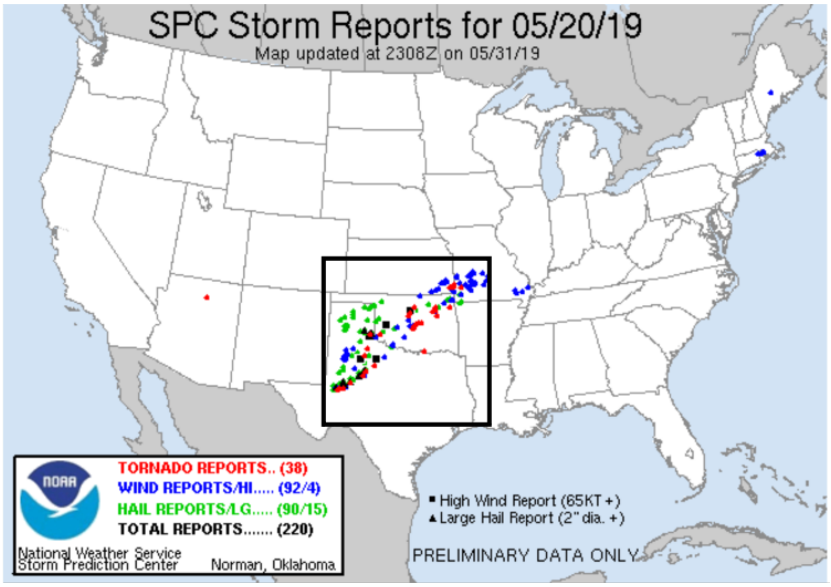

Figure 4.25: As in Fig. 4.1, except for 20 May 2019.

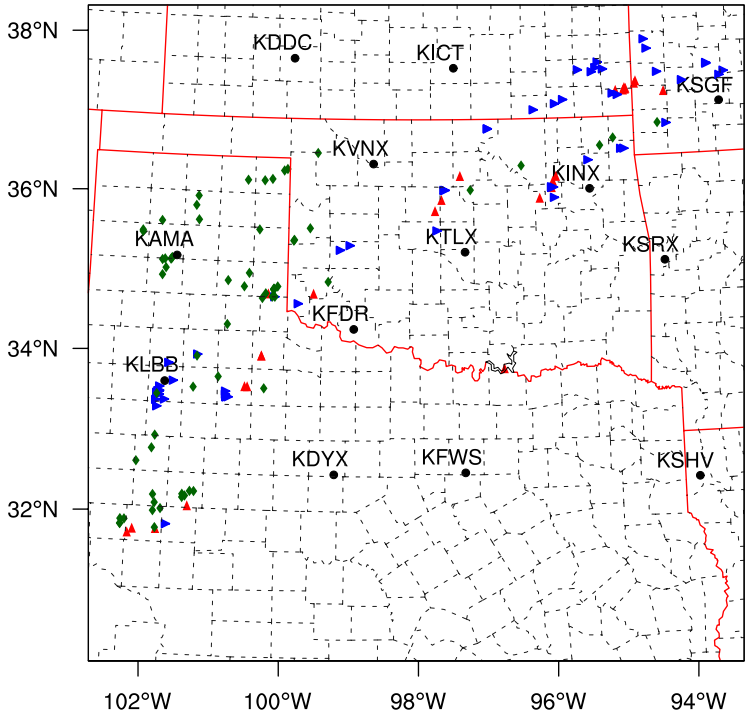

Figure 4.26: As in Fig. 4.2, except for 20 May 2019. The geographical center of the model simulation domain is at (34.32°N, 98.03°W).

4.3.1 **Results from comparison of experiments Q with Q_qv**

The forecasted composite reflectivity fields from experiments Q and Q_qv for 1-3 h forecasts initiated at 2300 UTC are presented together with observed composite reflectivity (Fig. 4.27). To better illustrate the differences between two experiments compared with the observations, three main regions are also marked and labeled as A, B and C from north to south in the simulation domain (Fig. 4.27a). At 0000 UTC (Fig. 4.27a), the observed composite reflectivity fields show that there are some weak cells in region A which grow quickly when they are moving northeastward. The two supercells in region B at 0000 UTC merge at 0100 UTC (Fig. 4.27d) and develop farther. Initially, there are two main cells in region C which split into several convective cells after a few hours. Moreover, a line of storms in central Oklahoma and south Kansas gradually propagates northeastward with new storm cells continuously forming and developing in the north and northeast of the simulation domain.

As for 1-3h forecasts, the composite reflectivity fields of Q and Q_qv behave very similar in terms of the reflectivity patterns. The convective cells in both Q and Q_qv move northeastward faster than that in the observed reflectivity fields. However, there still exists a slight difference between the two experiments. At 1-h forecast (valid at 0000 UTC), there are some spurious weak cells predicted at the border of Oklahoma and Arkansas in Q (Fig. 4.27b) which can be reduced in Q_qv (Fig. 4.27c). At 3-h forecast (valid at 0200 UTC), experiment Q (Fig. 4.27h) produces a storm cell in the southwest of the simulation domain while Q_qv does not (Fig. 4.27i).

The ETS and bias are calculated at every hour for 0-3h forecasts from 2000 UTC to 2300 UTC (2000, 2100, 2200 and 2300 UTC) with the thresholds of 20, 30 and 40 dBZ

in experiments Q and Q_qv (Fig. 4.28). Q_qv provides better analyses and forecasts with higher ETS values in comparison with Q for all thresholds (Figs. 4.28a, c, e). As for the bias, Q_qv performs better for closer to unity, especially at analysis time for all thresholds (Figs. 4.28b, d, f).

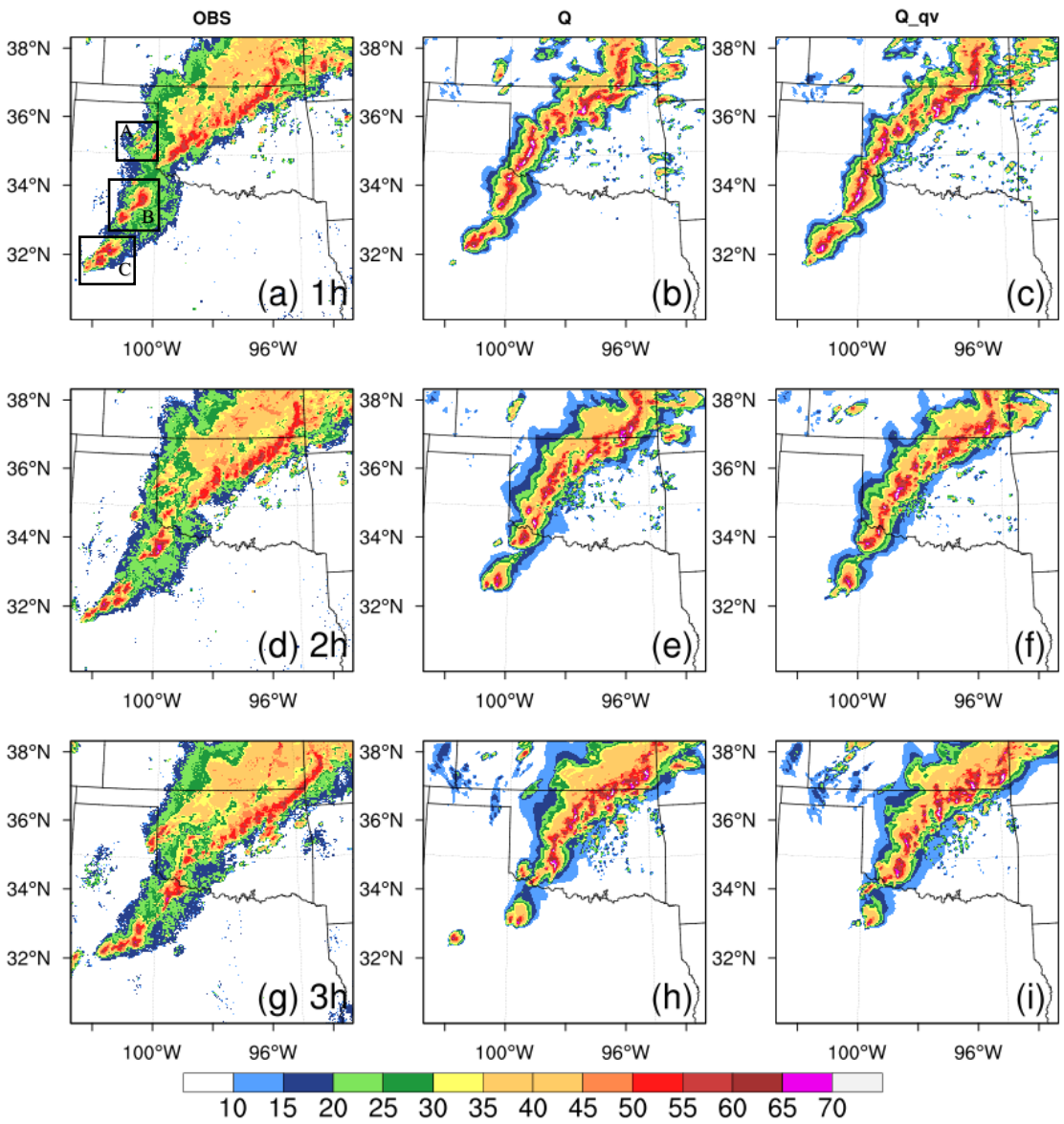

Figure 4.27: As in Fig. 4.3, except for 20 May 2019.

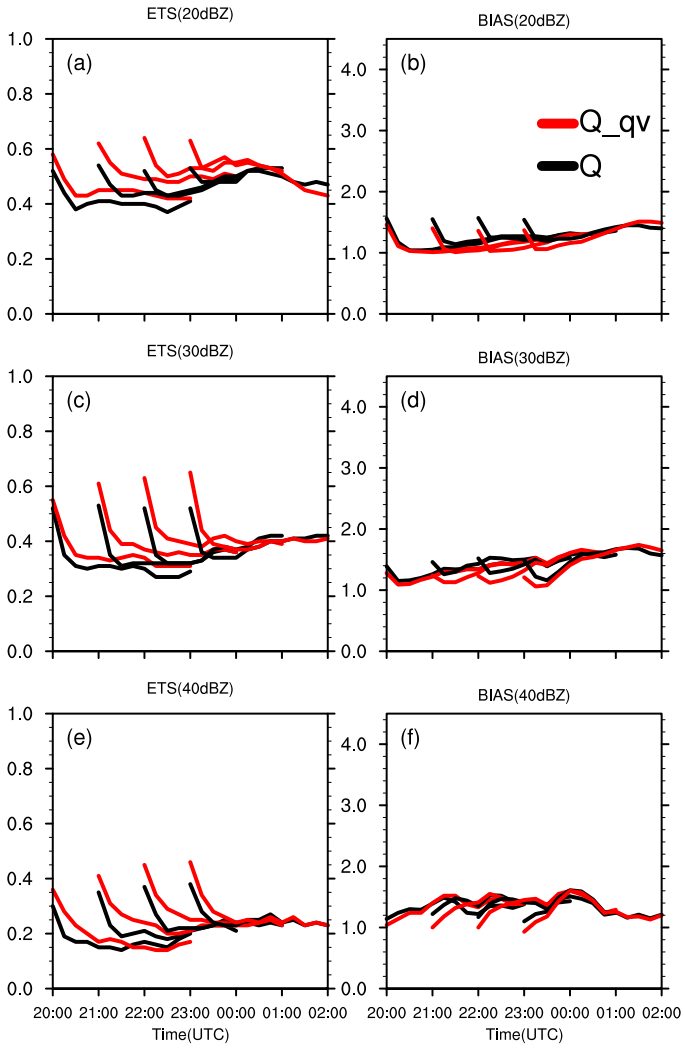

Figure 4.28: As in Fig. 4.4, except for 20 May 2019.

4.3.2 **Results from comparison of experiments Q_qv, LOGQ_qv and PQ_qv**

Same as two other cases, Q_qv, LOGQ_qv and PQ_qv are compared to examine the impact of different transformation functions. The analyzed and forecasted composite reflectivity fields from Q_qv, LOGQ_qv and PQ_qv for 0-3h forecasts initiated at 2300 UTC are displayed with the observed composite reflectivity fields in Fig. 4.29. Three main regions from north to south are marked and labeled as A, B and C to better illustrate the comparisons. At the analysis time (valid at 2300 UTC), the reflectivity patterns of three experiments are similar to the observed composite reflectivity fields (Fig. 4.29a) in term of storm locations. However, the storms are stronger in LOGQ_qv and PQ_qv (Figs. 4.29c, d) compared with that in Q_qv (Fig. 4.29b) and are more consistent with the observations (Fig. 4.29a). The analyzed reflectivity fields for LOGQ_qv and PQ_qv indicate that the three convective cells in region B are more vigorous than that for Q_qv, in better agreement with the observed reflectivity fields. There are several storm cells in region C which are very weak in Q_qv at 2300 UTC. In contrast, a cluster of several storm cells in region C from LOGQ_qv and PQ_qv are stronger which is closer to the observations.

For the 1-3h forecasts, the line of storms in all three experiments move northeastward faster than that in the observed reflectivity fields. At 1-h forecast (valid at 0000 UTC), there is a weak spurious cell predicted in Q_qv (Fig. 4.29f) at the border of Oklahoma and Kansas, which can be reduced in LOGQ_qv and PQ_qv (Figs. 4.29g, h). The spurious cell gradually develops and moves northward and, ultimately, outside of the simulation domain at 3-h forecast (valid at 0200 UTC, Fig. 4.29n). Overall, all the three experiments exhibit very similar forecast performance for composite reflectivity fields.

To further evaluate the performance of different transformation functions applied on hydrometeor mixing ratios as control variables, the composite maximum reflectivity swaths for 0-3h forecasts initiated at 2300 UTC are overlaid with the SPC storm reports in the simulation domain (Fig. 4.30). From the forecast beginning at 2300 UTC, the forecast reflectivity tracks are similar for all the experiments (Figs. 4.30b, c, d) and weaker than the observed reflectivity tracks (Fig. 4.30a). In addition, the three experiments all exhibit a large northeastward bias, especially for the storm tracks at the border of Texas and Oklahoma and the border of Oklahoma and Kansas, which is consistent with the conclusions drawn from the forecast composite reflectivity fields.

The ETS values are calculated at every hour for 0-3h forecasts from 2000 UTC to 2300 UTC with the thresholds of 20, 30 and 40 dBZ for all three experiments Q_qv, LOGQ_qv and PQ_qv to quantitatively investigate the performance (Fig. 4.31). At the analysis time, the ETS values for LOGQ_qv and PQ_qv are much higher than that for Q_qv for all thresholds which indicates that the analysis performance is quantitatively improved by using logarithmic and power transformed mixing ratios as control variables. However, for this case, LOGQ_qv outperforms PQ_qv at analysis time for the thresholds of 30 and 40 dBZ (Figs. 4.31b, c). For 0-3h forecasts, the contributions from LOGQ_qv and PQ_qv to the prediction are not obvious. For the 20 dBZ threshold (Fig. 4.31a), the ETS values for Q_qv are superior during the first 1-h forecast period. Totally, the three experiments have very similar ETS values for the 0-3h forecasts though the two experiments with logarithmic and power transformed mixing ratios as control variables are a little better in initial forecasts.

The RMSIs of radar radial velocity and reflectivity analyses for three experiments are also calculated (Fig. 4.32). For the RMSI of radial velocity, LOGQ_qv and PQ_qv exhibit great error reductions during the analysis steps when compared with Q_qv. For the RMSI of reflectivity, the patterns for error reduction are quite similar for all the three experiments. However, the forecast error growth is little faster in LOGQ_qv and PQ_qv than that in Q_qv for reflectivity.

The convergence rates for the experiments Q_qv and PQ_qv are compared to further examine the usefulness of power transformed function as hydrometeor control variables. The cost functions of total and individual parts are presented (Fig. 4.33). It is suggested that PQ_qv has faster convergence rates than Q_qv for total cost function and radial velocity observations (Figs. 4.33a, b). For reflectivity (Fig. 4.33c), Q_qv has faster convergence rates at the first 18 iteration steps. After 18 iterations, PQ_qv converges faster than Q_qv for reflectivity. Although blurred by oscillations of the cost function for pseudo-water vapor (Fig. 4.33d) at some iteration steps, the convergence rates of PQ_qv are faster than that of Q_qv most of times. In general, PQ_qv produces faster convergence rates in comparison with that of Q_qv.

To quantitatively evaluate the prediction skill for precipitation by using different control variables, the FSSs of 1-h accumulated precipitation for Q_qv and PQ_qv with different thresholds are calculated (Fig. 4.34). When the threshold increases from 1.0mm to 10.0mm, the scores decrease for both Q_qv and PQ_qv during each forecast period. Generally, Q_qv and PQ_qv exhibit very similar behavior. PQ_qv performs slightly better than Q_qv for the prediction skills. Fig. 4.35 shows the performance diagrams for 0-3h forecasts initiated at 2300 UTC with 20, 30 and 40 dBZ thresholds. At the analysis time

(Figs. 4.35a, b), PQ_qv produces higher CSI and SR value for reflectivity at all thresholds indicating the improvement of analysis in PQ_qv. As for 1-3h forecasts, Q_qv and PQ_qv exhibit very similar performance for all thresholds.

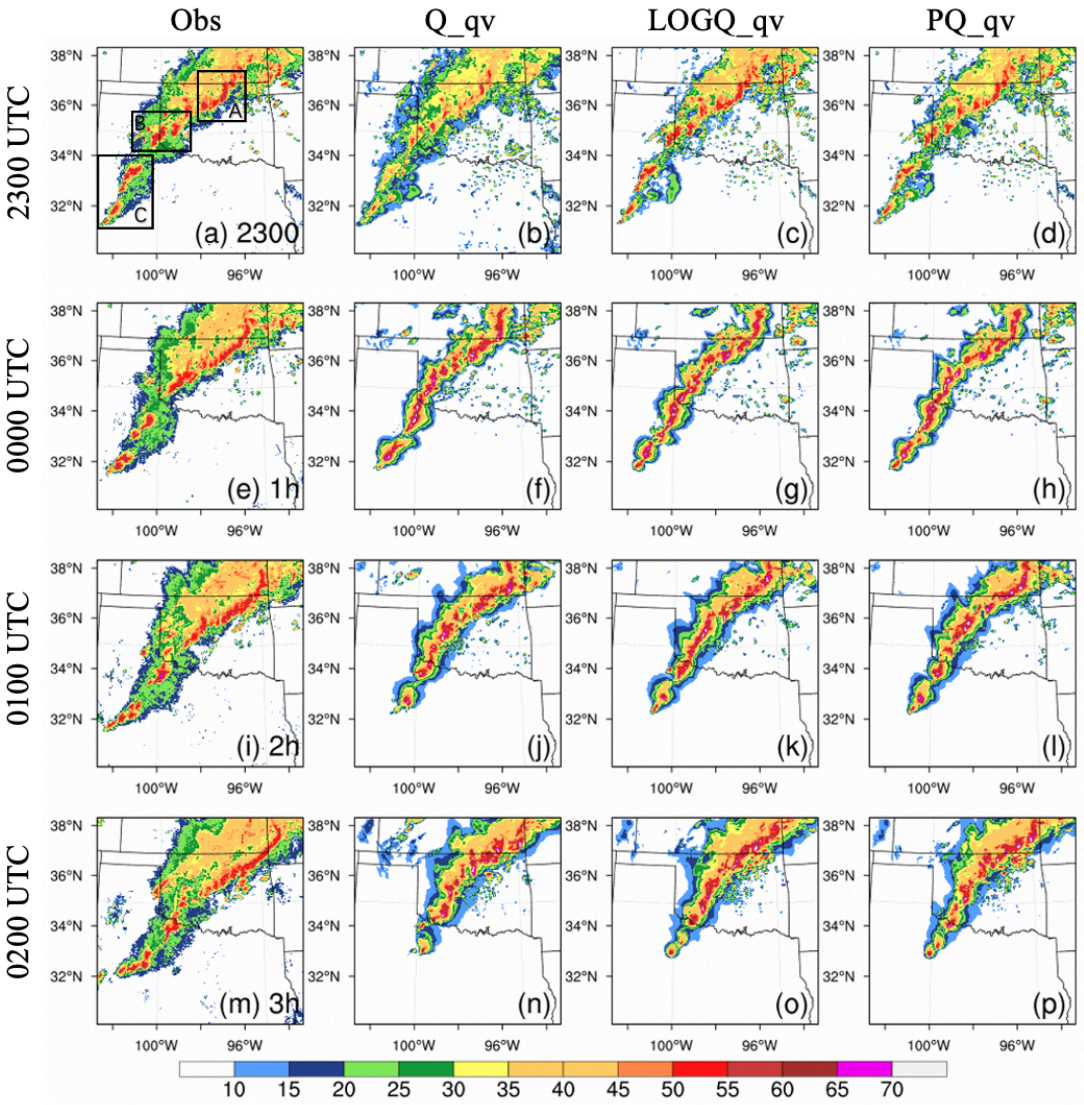

Figure 4.29: As in Fig. 4.5, except for 20 May 2019.

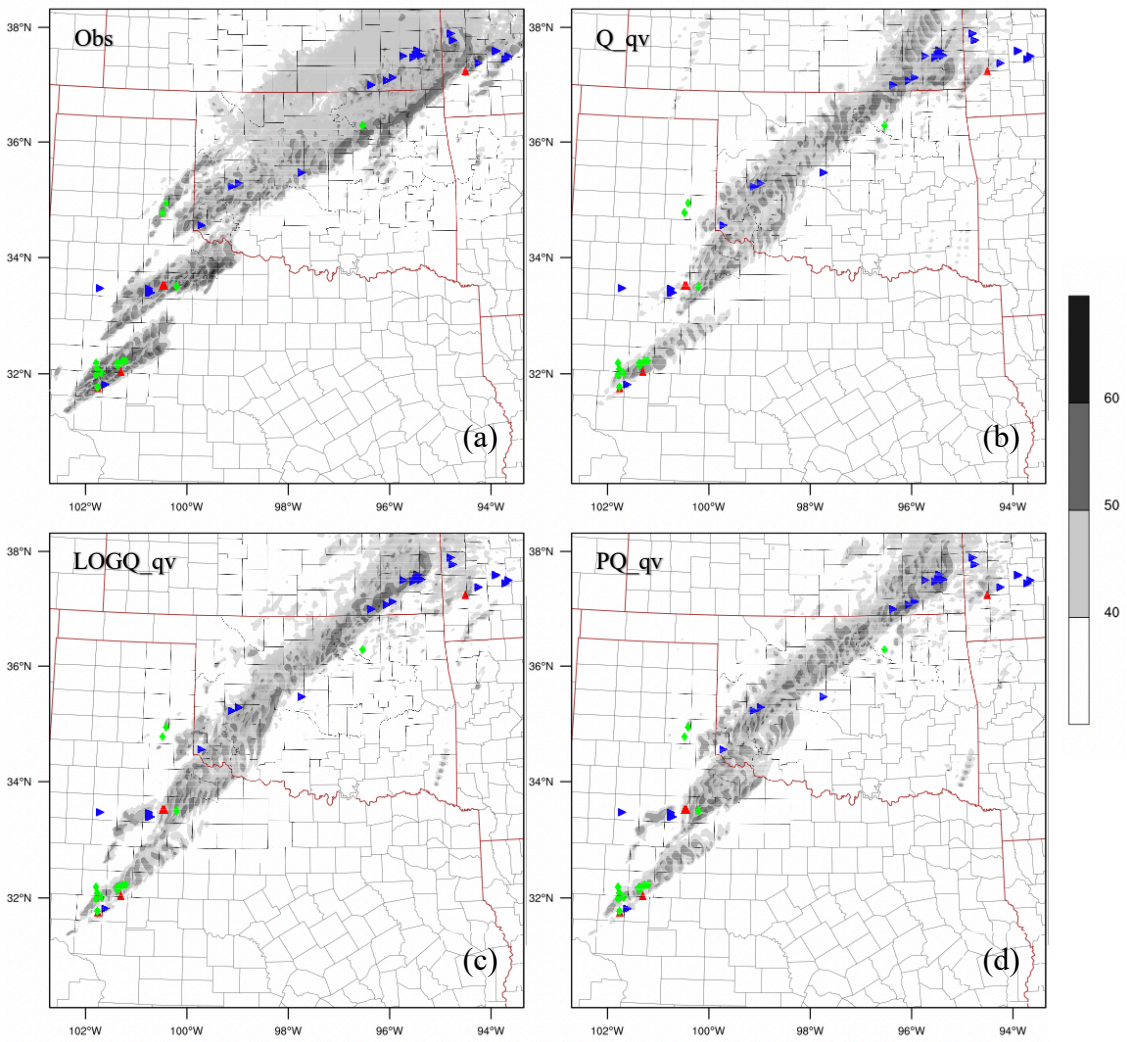

Figure 4.30: As in Fig. 4.6, except for 20 May 2019.

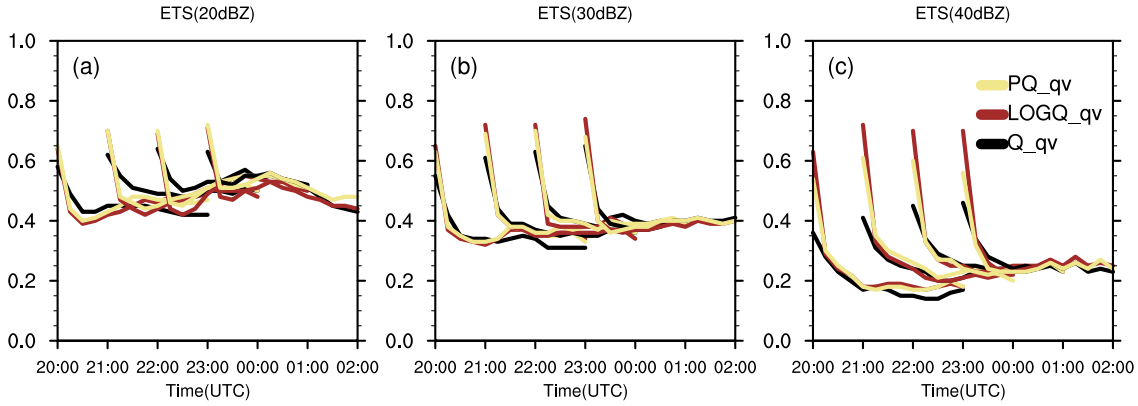

Figure 4.31: As in Fig. 4.7, except for 20 May 2019.

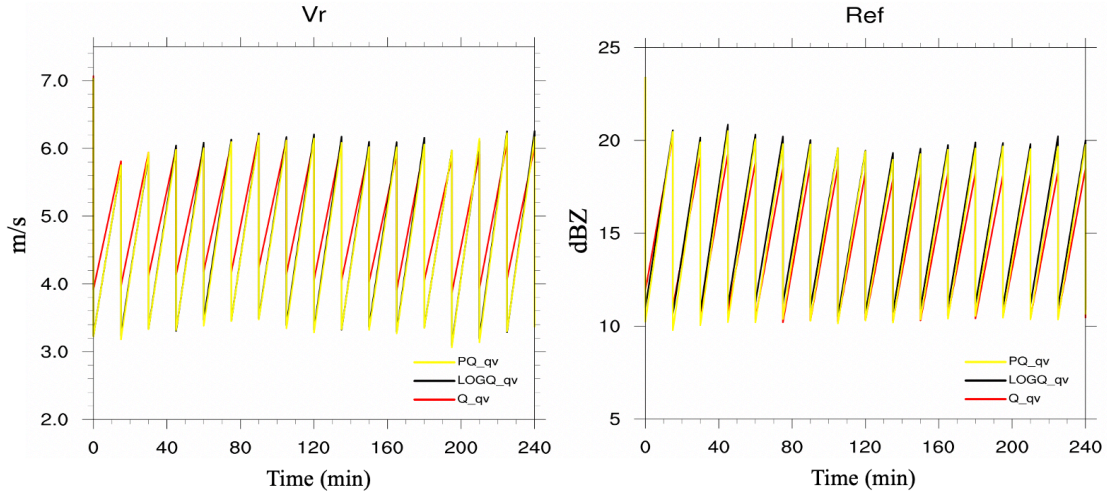

Figure 4.32: As in Fig. 4.8, except for 20 May 2019.

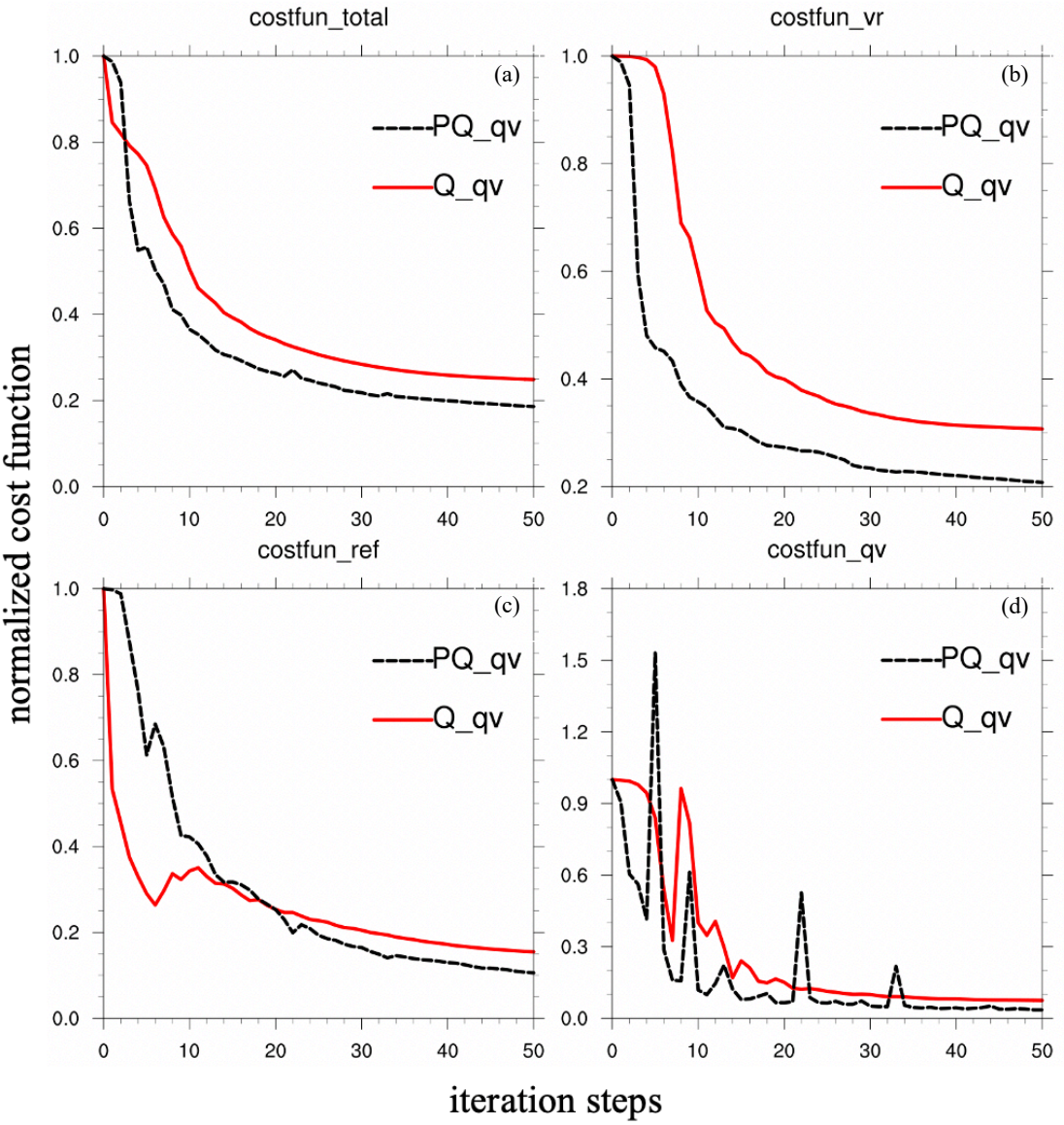

Figure 4.33: As in Fig. 4.9, except for 20 May 2019.

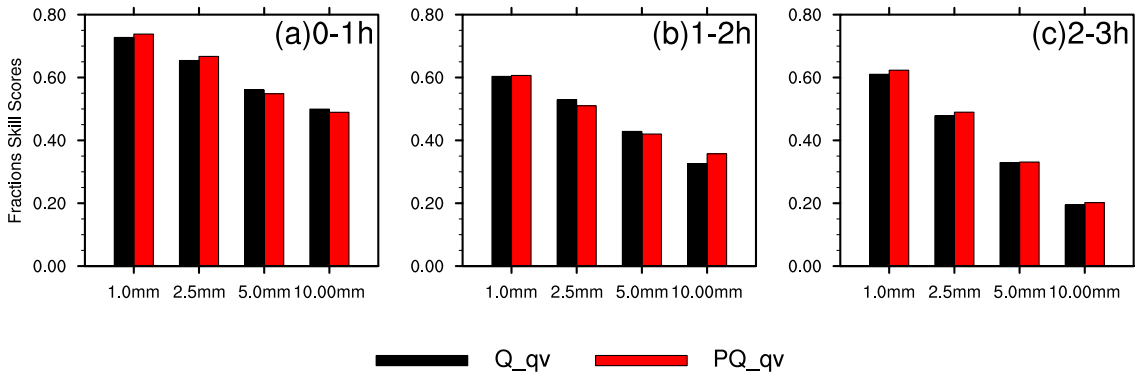

Figure 4.34: As in Fig. 4.10, except for 20 May 2019.

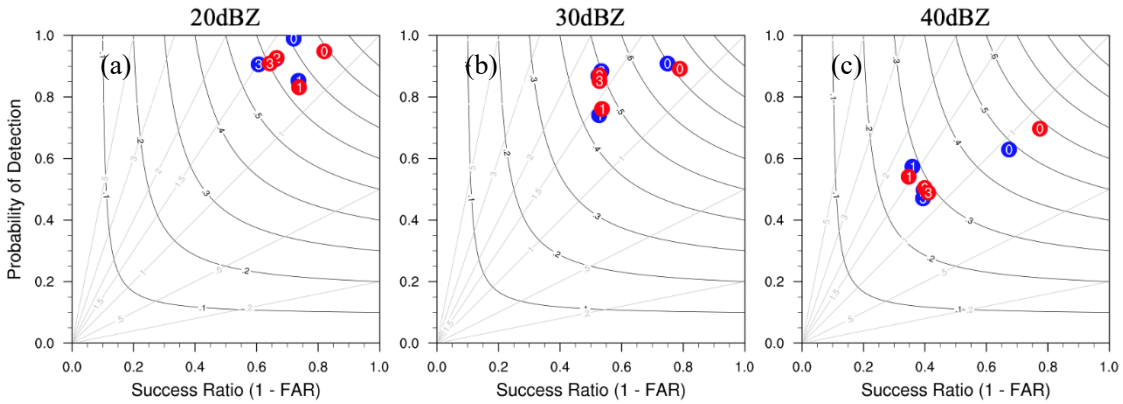

Figure 4.35: As in Fig. 4.11, except for 20 May 2019. The red and blue dots represent PQ_qv and Q_qv, respectively.

4.3.3 **Results from comparison of experiments PQ_qv with PQ_Pqv**

The power transformation functions are also applied on pseudo-water vapor observations to test whether it can help improve convective scale short term severe weather forecasts. The performance diagrams for 0-3h forecasts initiated at 2200 UTC and 2300 UTC for PQ_qv and PQ_Pqv are plotted (Fig. 4.36). For this case, the impact of applying power transformation function on pseudo-water vapor is also mixed. PQ_Pqv produces slightly lower CSI and SR values than that of PQ_qv, especially at 30 dBZ threshold (Figs. 4.36b, e). However, when it is initiated at 2300 UTC, the POD and CSI of PQ_Pqv are higher at the threshold of 40 dBZ (Fig. 4.36f). For the 1-3h forecasts, PQ_qv and PQ_Pqv show very similar performance at all thresholds.

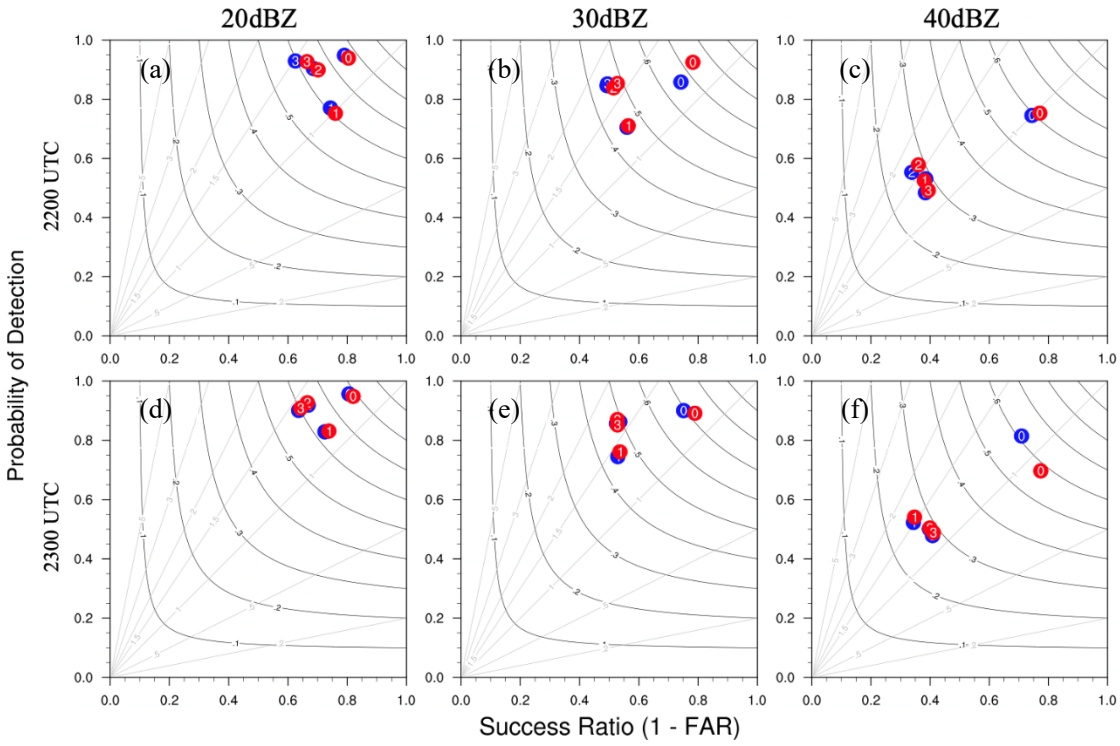

Figure 4.36: As in Fig. 4.12, except for 20 May 2019. The red and blue dots represent PQ_qv and PQ_Pqv, respectively.

5. Conclusions

Directly assimilating radar data in a variational framework has issues related to highly nonlinear radar reflectivity forward observation operator, especially with hydrometeor mixing ratios as control variables (Gao & Stensrud, 2012; Liu et al., 2020). Several approaches have been proposed to solve this issue. These include using logarithmic mixing ratios of hydrometeors as control variables (Carley, 2012), applying power transformation function on hydrometeors to form new control variables (Yang et al., 2020; Chen et al., 2020). In addition, a new algorithm to derive pseudo-water vapor observations from radar reflectivity has shown to be beneficial to the analyses and forecasts of convective storms (Lai et al., 2019).

As in Chen et al. (2020), they mainly focus on examining the performance with different values of parameter p through GSI En3DVar system. In this study, the impact of different transformation functions on the assimilation of radar data and pseudo-water vapor observations is tested within the 3DVAR system developed for NSSL WoF project (Gao et al., 2013). Three severe weather cases of 22 May, 28 May, and 20 May 2019 are tested to find out if the above methods can help improve the efficiency and accuracy of radar reflectivity DA and convective-scale short-term severe weather forecasts. Three major conclusions can be reached by this study.

5.1 Experiments Q vs Q_qv -- The usefulness of the pseudo water vapor

Experiments Q and Q_qv are compared to investigate the impact of pseudo-water vapor observations on short-term severe weather forecasts with three case studies which are generally representative for the severe weather events happened in the U.S. Mid-West

during the spring season. For the composite reflectivity forecasts, the convective cells in region B for the 22 May case and in region A, B and C for the 28 May case dissipate in Q but are predicted in Q_qv at 1-h forecast, which is more consistent with the reflectivity observations. Some spurious cells are predicted in Q but are reduced in Q_qv on 20 May. Therefore, the forecast performance is qualitatively improved by assimilating pseudo-water vapor observations.

To quantitatively examine the performance, the ETS and bias are calculated with different thresholds in Q and Q_qv. It is suggested that the ETS scores are enhanced in Q_qv when compared with Q for all the three cases. In addition, the forecasts in Q_qv has lower bias than that in Q. Overall, the assimilation of pseudo-water vapor observations qualitatively and quantitatively improves the analyses and 0-3h forecast performance of reflectivity. This conclusion further confirms the usefulness of assimilating pseudo-water vapor provided in Lai et al. (2019).

5.2 Experiments Q_qv, LOGQ_qv vs PQ_qv -- The usefulness of the application of the power transform function to hydrometeors

When using logarithmic and power transformed hydrometeor mixing ratios as control variables, the pseudo-water vapor observations are also assimilated along with radar data due to their positive impacts. Experiments Q_qv, LOGQ_qv and PQ_qv are compared to test the impact of different transformation functions on the short-term forecasts. For the composite reflectivity, the patterns are similar to the observations in terms of storm locations for all three experiments at the analysis time. However, the storm intensity differs from each experiment. Convective cells in LOGQ_qv and PQ_qv are

stronger in comparison with Q_qv, and in better agreement with the observed composite reflectivity. In addition, some spurious cells are produced in Q_qv for all the cases, which in the cases studied are comparatively reduced when applying LOGQ_qv and PQ_qv. For the 1-3h forecasts, all the three experiments exhibit very similar forecast performance for composite reflectivity. The composite reflectivity swaths for 0-3h forecasts show that the forecast reflectivity tracks are similar for all three types of experiments and are all weaker than the observed reflectivity tracks. However, there is a northeastward bias for the storm tracks on 20 May, a southward bias on 22 May and a northward bias on 28 May. The predicted composite reflectivity tracks in some regions are more consistent with the observations for PQ_qv with smaller phase errors compared with that of Q_qv, especially for the cases of 22 May and 28 May.

ETS values are calculated with different thresholds to quantitatively investigate the performance. For the three case studies examined, the ETS values for LOGQ_qv and PQ_qv are higher than that for Q_qv for all thresholds at the analysis time. Detailed analysis found variability in ETS values for PQ_qv and LOGQ_qv, depending on the case. PQ_qv outperforms LOGQ_qv with higher ETS values at the analysis time for the 22 May and 28 May cases. However, for the 20 May case, LOGQ_qv outperforms PQ_qv at the analysis time for the thresholds of 30 and 40 dBZ. For the 0-3h forecasts, the ETS values are similar for all three experiments. The RMSIs during the assimilation cycles show that LOGQ_qv and PQ_qv exhibit similar innovations which greatly reduces the errors associated with analyzed radial velocity when compared with Q_qv. For the RMSI of reflectivity, the forecast error growth is faster in LOGQ_qv and PQ_qv than in Q_qv.

The cost functions of total, radial velocity, reflectivity and pseudo-water vapor are normalized to compare the convergence rates. For the normalized cost function of radial velocity and pseudo-water vapor, PQ_qv has faster convergence rates than Q_qv. The FSSs of 1h accumulated precipitation with different thresholds are calculated to quantitatively evaluate the QPF skill. For the cases examined, PQ_qv outperforms Q_qv with higher FSS values for majority of thresholds, indicating better prediction skills for QPF by using power transformed mixing ratios as control variables. The performance diagrams represent the overall performance of the analysis and forecast. At the analysis time, PQ_qv produces higher CSI and SR for reflectivity at all thresholds. For the 1-3h forecasts, Q_qv and PQ_qv exhibit a similar performance for most thresholds.

Similar to Chen et al. (2020), using PQ as control variables produces the best analyses in terms of RMSIs and ETS. The convergence rate of PQ is also faster than Q as control variables. Furthermore, in this study, PQ is shown to have better prediction skills for QPF compared with that of Q. Instead of providing the best reflectivity forecasts with PQ as control variables in Chen et al. (2020), the forecast performance is very similar for all the three experiments in this study.

5.3 Experiments PQ_qv vs PQ_Pqv -- The usefulness of the application of power transformation functions to pseudo water vapor

Compared with previous studies, the power transformation functions are first applied to pseudo-water vapor observations to test whether it can help improve the convective-scale short term severe weather forecasts. The performance diagrams indicate that the impact of applying power transformation function on pseudo-water vapor is mixed with

lower CSI and SR values compared to PQ_qv for all thresholds at the analysis time. And these discrepancies between the experiments increase with the reflectivity threshold from 20 dBZ to 40 dBZ, especially for cases of 22 May and 28 May. For the 1-3h forecasts, the POD and SR values of PQ_Pqv are higher at all thresholds, especially for 2h and 3h forecast for 22 May cases. For the 20 May and 28 May cases, PQ_qv and PQ_Pqv show very similar performance for forecasts.

6. Future Research

The performance of using different transformation functions on hydrometeor variables and pseudo-water vapor observations, however, is only tested for three case studies during the same season and the same year. More cases from 2020 WoF spring experiments are available for study to see if the patterns explored in this study are representative. Furthermore, the power transformation function can be used in a pure or hybrid En3DVar DA system to test whether it shows positive impact when the ensemble information can be incorporated into the analysis and forecast system. The ensemble information may help make the analysis more balanced among different model variables. There still exists a few issues that need to be further investigated in the future work:

- Although using logarithmic and power transformed mixing ratios as control variables produces better analysis than hydrometeor mixing ratios themselves as control variables, the contributions from LOGQ and PQ to the prediction of severe weather storms are limited, which exhibit similar performances with the experiment Q. The reason for the mixed forecast performance may be related to the imbalance of the analyses of model variables which needs further examination in future studies. We will adopt 3DEnVar (Gao et al. 2014) to do more tests in the future.
- When the power transformation function is applied to the pseudo-water vapor observations, the analysis performance is mixed with lower CSI and SR values. The reason of affecting the analysis performance by using power transformed pseudo-water vapor also requires further investigation.

7. References

Brousseau, P., Seity, Y., Ricard, D., & Léger, J. (2016). Improvement of the forecast of convective activity from the AROME-France system: Improvement of Convective Activity Forecasts from AROME-France. Quarterly Journal of the Royal Meteorological Society, 142(699), 2231–2243. https://doi.org/10.1002/qj.2822

Buehner, M. (2005). Ensemble-derived stationary and flow-dependent background-error covariances: evaluation in a quasi-operational NWP setting. *Quart. J. Roy. Meteor. Soc.*, 131, 1013-1043.

Cao, Q., Zhang, G., Brandes, E. A., & Schuur, T. J. (2010). Polarimetric Radar Rain Estimation through Retrieval of Drop Size Distribution Using a Bayesian Approach. *Journal of Applied Meteorology and Climatology, 49*(5), 973–990. https://doi.org/10.1175/2009JAMC2227.1

Carley, J. R. (2012). Hybrid ensemble-3DVar radar data assimilation for the short-term prediction of convective storms. Theses and Dissertations Available from ProQuest, 1–206.

Caya, A., Sun, J., & Snyder, C. (2005). A Comparison between the 4DVAR and the Ensemble Kalman Filter Techniques for Radar Data Assimilation. Monthly Weather Review, 133(11), 3081–3094. https://doi.org/10.1175/MWR3021.1

Chen, L., Liu, C., Xue, M., Zhao, G., Kong, R., & Jung, Y. (2020). Use of Power Transform Mixing Ratios as Hydrometeor Control Variables for Direct Assimilation of Radar Reflectivity in GSI En3DVar and Tests with Five Convective Storms Cases. Monthly Weather Review. https://doi.org/10.1175/MWR-D-20-0149.1

Clark, A. J., Gallus, W. A., & Weisman, M. L. (2010). Neighborhood-Based Verification of Precipitation Forecasts from Convection-Allowing NCAR WRF Model Simulations and the Operational NAM. Weather and Forecasting, 25(5), 1495–1509. https://doi.org/10.1175/2010WAF2222404.1

Courtier, P., Thépaut, J.-N. and Hollingsworth, A., 1994: A strategy for operational implementation of 4D-Var, using an incremental approach. *Q. J. R. Meteorol. Soc*., **120,** 1367-1388.

Courtier, P., 1997: Dual formulation of four dimensional variational assimilation. *Quart. J. Roy. Meteor. Soc.,* **123,** 2449–2461.

Dowell, D. C., Wicker, L. J., & Snyder, C. (2011). Ensemble Kalman Filter Assimilation of Radar Observations of the 8 May 2003 Oklahoma City Supercell: Influences

of Reflectivity Observations on Storm-Scale Analyses. Monthly Weather Review, 139(1), 272–294. https://doi.org/10.1175/2010MWR3438.1

Gao, J., Xue, M., Shapiro, A., & Droegemeier, K. K. (1999). A Variational Method for the Analysis of Three-Dimensional Wind Fields from Two Doppler Radars. MONTHLY WEATHER REVIEW, 127, 15.

Gao, J., Xue, M., Brewster, K., & Droegemeier, K. K. (2004). A Three-Dimensional Variational Data Analysis Method with Recursive Filter for Doppler Radars. JOURNAL OF ATMOSPHERIC AND OCEANIC TECHNOLOGY, 21, 13.

Gao, J., & Stensrud, D. J. (2012). Assimilation of Reflectivity Data in a Convective-Scale, Cycled 3DVAR Framework with Hydrometeor Classification. Journal of the Atmospheric Sciences, 69(3), 1054–1065. https://doi.org/10.1175/JAS-D-11-0162.1**.**

Gao, J., T. M. Smith, D. J. Stensrud, C. Fu, K. Calhoun, K. L. Manross, J. Brogden, V. Lakshmanan, Y. Wang, K. W. Thomas, K. Brewster, and M. Xue, (2013a). A realtime weather-adaptive 3DVAR analysis system for severe weather detections and warnings with automatic storm positioning capability. ***Wea. Forecasting***, **28**, 727-745. http://dx.doi.org/10.1175/WAF-D-12-00093.1.

Gao, J., M. Xue**,** and D. J. Stensrud (2013b). The development of a hybrid EnKF-3DVAR algorithm for storm-scale data assimilation, *Adv. Meteor.* **2013**, 1-12, doi:10.1155/2013/512656.

Gao, J. and D. J. Stensrud. (2014) Some Observing System Simulation Experiments with a Hybrid 3DEnVAR System for Stormscale Radar Data Assimilation, *Mon. Wea. Rev.***, 142**, 3326-3346. http://dx.doi.org/10.1175/MWR-D-14-00025.1.

Gao, J., T. M. Smith, D. J. Stensrud, C. Fu, K. Calhoun, K. L. Manross, J. Brogden, V. Lakshmanan, Y. Wang, K. W. Thomas, K. Brewster, and M. Xue (2013). A realtime weather-adaptive 3DVAR analysis system for severe weather detections and warnings with automatic storm positioning capability. *Wea. Forecasting*, **28**, 727-745. http://dx.doi.org/10.1175/WAF-D-12-00093.1.

Gao, J., Fu, C., Stensrud, D. J., & Kain, J. S. (2016). OSSEs for an Ensemble 3DVAR Data Assimilation System with Radar Observations of Convective Storms. Journal of the Atmospheric Sciences, 73(6), 2403–2426. https://doi.org/10.1175/JAS-D-15-0311.1

Gilmore, M. S., Straka, J. M., & Rasmussen, E. N. (2004). Precipitation Uncertainty Due to Variations in Precipitation Particle Parameters within a Simple Microphysics Scheme. Monthly Weather Review, 132(11), 2610–2627. https://doi.org/10.1175/MWR2810.1

Gustafsson, N., Janjić, T., Schraff, C., Leuenberger, D., Weissmann, M., Reich, H., et al. (2018). Survey of data assimilation methods for convective-scale numerical weather prediction at operational centres. *Quarterly Journal of the Royal Meteorological Society*, *144*(713), 1218–1256. https://doi.org/10.1002/qj.3179

Hamill, T. M., & Snyder, C. (2000). A Hybrid Ensemble Kalman Filter–3D Variational Analysis Scheme. MONTHLY WEATHER REVIEW, 128, 15.

Hong, S.-Y., Noh, Y., & Dudhia, J. (2006). A New Vertical Diffusion Package with an Explicit Treatment of Entrainment Processes. Monthly Weather Review, 134(9), 2318–2341. https://doi.org/10.1175/MWR3199.1

Hu, M., Xue, M., & Brewster, K. (2006a). 3DVAR and Cloud Analysis with WSR-88D Level-II Data for the Prediction of the Fort Worth, Texas, Tornadic Thunderstorms. Part I: Cloud Analysis and Its Impact. Monthly Weather Review, 134(2), 675–698. https://doi.org/10.1175/MWR3092.1

Hu, M., Xue, M., Gao, J., & Brewster, K. (2006b). 3DVAR and Cloud Analysis with WSR-88D Level-II Data for the Prediction of the Fort Worth, Texas, Tornadic Thunderstorms. Part II: Impact of Radial Velocity Analysis via 3DVAR. Monthly Weather Review, 134(2), 699–721. https://doi.org/10.1175/MWR3093.1

Iacono, M. J., Delamere, J. S., Mlawer, E. J., Shephard, M. W., Clough, S. A., & Collins, W. D. (2008). Radiative forcing by long-lived greenhouse gases: Calculations with the AER radiative transfer models. Journal of Geophysical Research, 113(D13), D13103. https://doi.org/10.1029/2008JD009944

Johnson, A., Wang, X., Carley, J. R., Wicker, L. J., & Karstens, C. (2015). A Comparison of Multiscale GSI-Based EnKF and 3DVar Data Assimilation Using Radar and Conventional Observations for Midlatitude Convective-Scale Precipitation Forecasts. Monthly Weather Review, 143(8), 3087–3108. https://doi.org/10.1175/MWR-D-14-00345.1

Kalnay, E. (2003). Atmospheric modeling, data assimilation and predictability, 369.

Kong, R., Xue, M., & Liu, C. (2018). Development of a Hybrid En3DVar Data Assimilation System and Comparisons with 3DVar and EnKF for Radar Data Assimilation with Observing System Simulation Experiments. Monthly Weather Review, 146(1), 175–198. https://doi.org/10.1175/MWR-D-17-0164.1

Kong, R., Xue, M., Liu, C., & Jung, Y. (2020). Comparisons of Hybrid En3DVar with 3DVar and EnKF for Radar Data Assimilation: Tests with the 10 May 2010 Oklahoma Tornado Outbreak. Monthly Weather Review, 1–60. https://doi.org/10.1175/MWR-D-20-0053.1

Lai, A., Gao, J., Koch, S. E., Wang, Y., Pan, S., Fierro, A. O., et al. (2019). Assimilation of Radar Radial Velocity, Reflectivity, and Pseudo–Water Vapor for Convective-

Scale NWP in a Variational Framework. Monthly Weather Review, 147(8), 2877–2900. https://doi.org/10.1175/MWR-D-18-0403.1

Lilly, D. K. (1990). Numerical prediction of thunderstorms—has its time come? Quarterly Journal of the Royal Meteorological Society, 116(494), 779–798. https://doi.org/10.1002/qj.49711649402

Lin, Y. (2011). GCIP/EOP Surface: Precipitation NCEP/EMC 4KM Gridded Data (GRIB) Stage IV Data. Version 1.0 (Version 1.0) [GNU Zip Compressed (.gz) Gridded Binary (GRIB) Format (application/x-gzip),GNU Zip (.gz) Format (application/x-gzip)]. UCAR/NCAR - Earth Observing Laboratory. https://doi.org/10.5065/D6PG1QDD

Lin, Y.-L., Farley, R. D., & Orville, H. D. (1983). Bulk Parameterization of the Snow Field in a Cloud Model. Journal of Climate and Applied Meteorology, 22(6), 1065–1092.

Liu, C., Xue, M., & Kong, R. (2019). Direct Assimilation of Radar Reflectivity Data Using 3DVAR: Treatment of Hydrometeor Background Errors and OSSE Tests. Monthly Weather Review, 147(1), 17–29. https://doi.org/10.1175/MWR-D-18-0033.1

Liu, C., Xue, M., & Kong, R. (2020). Direct Variational Assimilation of Radar Reflectivity and Radial Velocity Data: Issues with Nonlinear Reflectivity Operator and Solutions. MONTHLY WEATHER REVIEW, 148, 20.

Lorenc, A. C. (1986). Analysis methods for numerical weather prediction. Quarterly Journal of the Royal Meteorological Society, 112(474), 1177–1194. https://doi.org/10.1002/qj.49711247414

Lorenc, A., 2003: The potential of the ensemble Kalman filter for NWP - a comparison with 4DVar. *Quart. J. Roy. Meteor. Soc.*, 129, 3183-3204.

Purser, R. J., W.-S. Wu, D. Parrish, and N. M. Roberts, 2003: Numerical aspects of the application of recursive filters to variational statistical analysis. Part I: Spatially homogeneous and isotropic Gaussian covariances. *Mon. Wea. Rev.,* **131,** 1524–1535.

Roberts, N. M., & Lean, H. W. (2008). Scale-Selective Verification of Rainfall Accumulations from High-Resolution Forecasts of Convective Events. Monthly Weather Review, 136(1), 78–97. https://doi.org/10.1175/2007MWR2123.1

Roebber, P. J. (2009). Visualizing Multiple Measures of Forecast Quality. Weather and Forecasting, 24(2), 601–608. https://doi.org/10.1175/2008WAF2222159.1

Schenkman, A. D., Xue, M., Shapiro, A., Brewster, K., & Gao, J. (2011). The Analysis and Prediction of the 8–9 May 2007 Oklahoma Tornadic Mesoscale Convective System by Assimilating WSR-88D and CASA Radar Data Using 3DVAR. Monthly Weather Review, 139(1), 224–246. https://doi.org/10.1175/2010MWR3336.1

Simonin, D., S. P. Ballard, and Z. Li, 2014: Doppler radar radial wind assimilation using an hourly 874 cycling 3d-var with a 1.5 km resolution version of the met office unified model for nowcasting. Quart. J. Roy. Meteor. Soc., 140 (684), 2298–2314, doi:10.1002/qj.2298

Smith, P. L., Myers, C. G., & Orville, H. D. (1975). Radar Reflectivity Factor Calculations in Numerical Cloud Models Using Bulk Parameterization of Precipitation. Journal of Applied Meteorology and Climatology, 14(6), 1156–1165. https://doi.org/10.1175/1520-0450(1975)014<1156:RRFCIN>2.0.CO;2

Stensrud, D. J., & Gao, J. (2010). Importance of Horizontally Inhomogeneous Environmental Initial Conditions to Ensemble Storm-Scale Radar Data Assimilation and Very Short-Range Forecasts. Monthly Weather Review, 138(4), 1250–1272. https://doi.org/10.1175/2009MWR3027.1

Stensrud, D.J., Wicker, L.J., Xue, M., Dawson II, D.T., Yussouf, N., Wheatley, D.M., Thompson, T.E., Snook, N.A., Smith, T.M., Schenkman, A.D. and Potvin, C.K. (2013) Progress and challenges with Warn-on-Forecast. *Atmospheric Research*, 123, pp.2-16.

Sugimoto, S., Crook, N. A., Sun, J., Xiao, Q., & Barker, D. M. (2009). An Examination of WRF 3DVAR Radar Data Assimilation on Its Capability in Retrieving Unobserved Variables and Forecasting Precipitation through Observing System Simulation Experiments. Monthly Weather Review, 137(11), 4011–4029. https://doi.org/10.1175/2009MWR2839.1

Sun, J., & Crook, N. A. (1997). Dynamical and Microphysical Retrieval from Doppler Radar Observations Using a Cloud Model and Its Adjoint. Part I: Model Development and Simulated Data Experiments. JOURNAL OF THE ATMOSPHERIC SCIENCES, 54, 20.

Sun, J., & Wang, H. (2013). Radar Data Assimilation with WRF 4D-Var. Part II: Comparison with 3D-Var for a Squall Line over the U.S. Great Plains. Monthly Weather Review, 141(7), 2245–2264. https://doi.org/10.1175/MWR-D-12-00169.1

Sun, J., Flicker, W., & Lilly, K. (1991). Recovery of three-dimensional wind and temperature fields from simulated single-doppler radar data. Journal of the Atmospheric Sciences, 876–890. https://doi.org/10.1175/1520-0469(1991)048<0876:ROTDWA>2.0.CO;2

Tewari, M., Wang, W., Dudhia, J., LeMone, M. A., Mitchell, K., Ek, M., et al. (2016). Implementation and verification of the united NOAH land surface model in the WRF model. 20th Conference on Weather Analysis and Forecasting/16th Conference on Numerical Weather Prediction (p. 15).

Thompson, G., Field, P. R., Rasmussen, R. M., & Hall, W. D. (2008). Explicit Forecasts of Winter Precipitation Using an Improved Bulk Microphysics Scheme. Part II: Implementation of a New Snow Parameterization. Monthly Weather Review, 136(12), 5095–5115. https://doi.org/10.1175/2008MWR2387.1

Tong, M., & Xue, M. (2005). Ensemble Kalman Filter Assimilation of Doppler Radar Data with a Compressible Nonhydrostatic Model: OSS Experiments. Monthly Weather Review, 133(7), 1789–1807. https://doi.org/10.1175/MWR2898.1

Wang, H., Sun, J., Zhang, X., Huang, X.-Y., & Auligné, T. (2013). Radar Data Assimilation with WRF 4D-Var. Part I: System Development and Preliminary Testing. Monthly Weather Review, 141(7), 2224–2244. https://doi.org/10.1175/MWR-D-12-00168.1

Wang, X., C. Snyder, and T. M. Hamill (2007). On the theoretical equivalence of differently proposed ensemble/3D-Var hybrid analysis schemes. *Mon. Wea. Rev*. **135**, 222-227.

Wang, Y., & Wang, X. (2017). Direct Assimilation of Radar Reflectivity without Tangent Linear and Adjoint of the Nonlinear Observation Operator in the GSI-Based EnVar System: Methodology and Experiment with the 8 May 2003 Oklahoma City Tornadic Supercell. Monthly Weather Review, 145(4), 1447–1471. https://doi.org/10.1175/MWR-D-16-0231.1

Xiao, Q., Kuo, Y.-H., Sun, J., Lee, W.-C., Lim, E., Guo, Y.-R., & Barker, D. M. (2005). Assimilation of Doppler Radar Observations with a Regional 3DVAR System: Impact of Doppler Velocities on Forecasts of a Heavy Rainfall Case. Journal of Applied Meteorology, 44(6), 768–788. https://doi.org/10.1175/JAM2248.1

Yang, R., Purser, R. J., & Carley, J. R. (2020). Application of a nonlinear transformation function to the variational analysis of visibility and ceiling height. https://doi.org/10.25923/ESW8-5N84

Yussouf, N., Mansell, E. R., Wicker, L. J., Wheatley, D. M., & Stensrud, D. J. (2013). The Ensemble Kalman Filter Analyses and Forecasts of the 8 May 2003 Oklahoma City Tornadic Supercell Storm Using Single- and Double-Moment Microphysics Schemes. Monthly Weather Review, 141(10), 3388–3412. https://doi.org/10.1175/MWR-D-12-00237.1